Lawley, C.J.M.; Selby, D.; **Condon, D.**; Imber, J.. 2014 Palaeoproterozoic orogenic gold style mineralization at the Southwestern Archaean Tanzanian cratonic margin, Lupa Goldfield, SW Tanzania: implications from U–Pb titanite geochronology. *Gondwana Research*, 26 (3-4). 1141-1158. 10.1016/j.gr.2013.08.025

Palaeoproterozoic Orogenic Gold Style Mineralization at the Southwestern Archaean Tanzanian Cratonic Margin, Lupa Goldfield, SW Tanzania: Implications from U-Pb Titanite Geochronology

C.J.M. Lawley[1,2*], D. Selby[1], D. Condon[3] and J. Imber[1]

[1]Department of Earth Sciences, Durham University, Science Labs, Durham, DH1 3LE, UK
[2]Natural Resources Canada, Geological Survey of Canada, Ottawa, Ontario, K1A 0E8, Canada
[3]Natural Environment Research Council Isotope Geosciences Laboratory, British Geological Survey, Keyworth, Nottingham, NG12 5GG, UK

*corresponding author: e-mail: clawley@NRCan.gc.ca; Tel: 1 (613) 996-23593

Abstract: The Lupa Goldfield, situated at the southwestern Tanzanian cratonic margin, comprises a network of auriferous quartz veins and greenschist facies mylonitic shear zones cutting a suite of Archaean-Palaeoproterozoic granitic-gabbroic intrusions. The existing geochronological database points to a protracted, but episodic 1.96−1.88 Ga magmatic history that is broadly coincident with the 2.1–1.8 Ga Ubendian Orogeny. Molybdenite, pyrite and chalcopyrite samples from mineralized quartz veins and mylonitic shear zones yield Re-Os model ages that range from 1.95–1.88 Ga, whereas ca. 1.88 Ga pyrite with gold bearing inclusions and sampled from the host mylonitic shear zone suggest that gold occurred relatively late in this hydrothermal history. The ca. 1.88 Ga gold event is recorded at all five of the studied prospects, whereas the relationship between gold and the disparately older 1.95 and 1.94 Ga Re-Os molybdenite ages is unclear. New U-Pb metamorphic titanite dating of a foliated Archaean granite sample (ca. 2.76 Ga) suggests that the onset of ductile deformation within the Lupa Goldfield occurred at ca. 1.92 Ga, and some ca. 40 Myr prior to auriferous and brittle-ductile mylonitic shear zones at ca. 1.88 Ga. Early ductile deformation is not associated with gold mineralization, but the ductile deformation fabrics and, in particular the development of rheologically weak chloritic folia, may have acted as zones of pre-existing weakness that localized strain and influenced the geometry of later auriferous mylonitic shear zones. The large age difference between U-Pb zircon and titanite ages for the Archaean granite sample is in contrast to new U-Pb titanite ages for the Saza Granodiorite (1930 ± 3 Ma), which are only slightly outside of analytical uncertainty at the 2σ level with a previously reported U-Pb zircon age for the same sample (1935 ± 1 Ma). These new age results, together with previously reported U-Pb and Re-Os ages, highlight the protracted magmatic, hydrothermal and structural evolution of the Lupa Goldfield (1.96–1.88 Ga). They are also consistent with other palaeo-convergent margins where orogenic gold systems genesis occurs relatively late in the orogen's tectono-thermal history.

Keywords: Lupa Goldfield, Paleoproterozoic, Orogenic Gold, Tanzania, Ubendian Belt

1.0 Introduction

1.1 Tanzanian gold deposits

Tanzania represents the fourth largest gold producer in Africa and is the subject of renewed mineral exploration interest since the introduction of reformed mining legislation in the late 1990s (Roe and Essex, 2009; Yager, 2010; Brown et al., 2013). The vast majority of gold production and mineral exploration are concentrated in northern Tanzania and the Lake Victoria Goldfield where world-class deposits (i.e., deposits with ≥ 3.0 Moz of contained gold in proven and probable reserves) such as Geita (12.3 Moz; AngloGold Ashanti Annual Report, 2012) and Bulyanhulu (8.0 Moz; Barrick Annual report, 2012) are located (Fig. 1). Two other operating mines are also located in the Lake Victoria Goldfields [North Mara, 2.2 Moz (Barrick Annual report, 2012); Buzwagi, 2.0 Moz (Barrick Annual Report, 2012)] in addition to past producing mines (e.g., Golden Pride, Tulawaka) and numerous smaller-scale artisanal mining operations (Fig. 1). These deposits are hosted by Neoarchaean greenschist-amphibolite facies granite-greenstone belts and lesser sedimentary successions comprising the Tanzanian Craton and are typical of similarly-aged orogenic gold deposits worldwide (e.g., Goldfarb et al., 2001).

The Lake Victoria Goldfield represents merely one example of Tanzania's gold endowed regions (Fig. 1). Metamorphic belts contiguous with the Tanzanian Craton host a variety of lesser known goldfields (e.g., Lupa, Mpanda, Mbinga and Niassa) that have attracted comparatively less modern gold exploration. The geologic settings of these goldfields also remain poorly understood despite their historic importance during Tanzania's colonial period and on-going artisanal mining activity (van Straaten, 1984; Kuehn et al., 1990). Recent geochronology studies suggest that several of the metamorphic belts hosting these goldfields have a complex tectono-thermal history spanning multiple orogenic cycles (e.g., Boniface et al., 2012, Boniface and Schenk, 2012). As a result, linking deformation, magmatism, and mineralization to a particular orogenic cycle is equivocal in the absence of precise geochronologic constraints. In this contribution, we report new U-Pb titanite age constraints on the earliest deformation fabrics ("D1" – see below) recognized within the western Lupa Goldfield, SW Tanzania. Together the available data suggest that Proterozoic-Palaeozoic metamorphic belts surrounding the Archaean Tanzanian Craton represent highly prospective regions and possess hitherto unrecognized gold potential.

1.2 Chronology of gold deposits hosted by metamorphic belts

Determining the absolute ages of magmatism, metamorphism and mineralization at gold deposits hosted by metamorphic belts is the subject of concentrated study and continuing controversy (e.g., Groves et al., 2003). Establishing the timing of mineralization is particularly challenging due to the dearth of suitable minerals for traditional geochronologic methods. Nevertheless, recent advances in unconventional sulphide (Stein et al., 2000; Morelli et al., 2007), hydrothermal phosphate (Şener et al., 2005; Vielreicher et al., 2010) and titanite (Lin and Corfu, 2002) geochronometers has dramatically improved our understanding of metallogenic time scales and processes at paleo-convergent margins. Re-Os geochronology studies (i.e., Re-Os dating of sulphide minerals presumed to be co-genetic with gold) have proven to be a particularly effective approach and have provided unequivocal examples of gold mineralization concomitant with magmatic intrusions at the million-year time scale (Morelli et al., 2007; Ootes et al., 2007; 2011; Lawley et al., in press-a). These studies add to a rapidly expanding global database of geochronologic ages that demonstrate broad contemporaneity between the absolute timing of gold and magmatism at most world-class goldfields (e.g., Witt and Vanderhor, 1998; Kerrich and Wyman, 1990; Kerrich and Cassidy, 1994; Kerrich and Kyser, 1994; Oberthur et al., 1998; Arne et al., 2001; Davis and Lin, 2003; Bucci et al., 2004; Bierlein et al., 2009; Dziggel et al., 2010; McFarlane et al., 2011).

The temporal relationship between magmatism and gold mineralization has led to the intrusion-related deposit model and is cited as evidence for the importance of locally derived magmatic hydrothermal fluids in the development of epigenetic gold deposits hosted by metamorphic belts at convergent margins (Sillitoe and Thompson, 1998; Lang and Baker, 2001). The inference of locally derived magmatic hydrothermal fluids is at odds with orogenic gold deposits, which are associated with a similar geodynamic setting (i.e., convergent margins), but are related to distal hydrothermal fluids of probable metamorphic origin (e.g., Groves et al., 1998; Groves et al., 2003; Phillips and Powell, 2010). Previous attempts at addressing this controversy have employed a variety of isotopic tracers, but have provided contrasting results due to, in part, the difficulty in discriminating isotopically distinct fluid sources after the fluid-rock interaction that characterizes most hydrothermal systems (e.g., Ridley and Diamond, 2000; Salier et al., 2005; Fu et al., 2012).

The recent emphasis placed on the role of metal-rich magmatic fluids emanating from mid- to lower-crustal magmatic systems also raises the possibility of distally (e.g., lower crustal) derived magmatic fluids contributing to hydrothermal systems operating at higher crustal levels (Botcharnikov et al., 2011; Hronsky et al., 2012). Whilst the genetic relationship between magmatic hydrothermal fluids and gold is satisfactorily demonstrated at several deposits (e.g., Hemlo; Davis and Lin, 2003), the exact role of magmatism and magmatically derived hydrothermal fluids in the development of epigenetic gold mineralization remains uncertain at most metamorphic belts (e.g., Charter Towers; Kreuzer, 2005). However, precise geochronologic constraints on magmatism and mineralization in conjunction with isotopic and fluid inclusions studies remain important tools in further constraining ore deposit models (Rasmussen et al., 2006).

Gold deposits and prospects in the Lupa Goldfield occur within a Palaeoproterozoic magmatic arc at the Tanzanian cratonic margin and thus share a close spatial and temporal relationship with granitic-gabbroic intrusions (Manya, 2011; Lawley et al., 2013). This spatial and temporal association between magmatism and mineralization has led to the suggestion that the gold prospects of the Lupa Goldfield are typical of the intrusion-related deposit type (Manya, 2012). In contrast, the protracted hydrothermal history (Lawley et al., in press-a) coupled with the structural setting of the deposits (Lawley et al., in press-b) suggests that these deposits share more similarities with orogenic style gold mineralization. In this contribution we report new U-Pb titanite ages, which provide new constraints on the onset of deformation at the Lupa Goldfield. This, coupled with the available Re-Os and U-Pb ages allows a critical evaluation of ore deposit models for gold prospects within the Lupa Goldfield.

2.0 Regional Geology

2.1 Tanzanian Craton and contiguous metamorphic belts

The Tanzanian Craton extends from central to northern Tanzania and into southwestern Kenya and southeastern Uganda (Fig. 1). Previous workers divided the Archaean Tanzanian craton into three ‘Systems’ (e.g., Cahen et al., 1984) or ‘Supergroups’ (e.g., Borg and Krogh, 1999): 1) the Dodoman of central Tanzania, which comprises high-grade gneiss, migmatitic rocks, and granitic-granodioritic intrusions; 2) the Nyanzian of northern Tanzania, which comprises greenschist-amphibolite facies meta-volcanic rocks, lesser meta-sedimentary successions and granitic intrusions; and 3) the Kavirondian, which unconformably overlies the Nyanzian and comprises greenschist-amphibolite facies meta-sedimentary successions (for additional details regarding the geology, age and nomenclature of the Tanzanian Craton readers are referred to reviews by Clifford, 1970; Bell and Dodson, 1981; Cahen et al., 1984; Borg and Krogh, 1989; Borg and Shackleton, 1997). However, more recent geologic and geochronological data sets suggest that the Nyanzian System comprises multiple temporally and geochemically distinct volcano-stratigraphic sequences, which should not be regarded as a single stratigraphic package (Manya et al., 2006). Moreover, the Tanzanian Cratons's tectonic framework is likely more complex than previously suggested and can be further subdivided into thirteen broadly WNW-ESE trending superterranes [Fig. 1; East Lake Victoria Superterrane (ELVST); Mwanza-Lake Eyasi Superterrane (MLEST); Lake Nyanza Superterrane (LNST); Moyowosi-Manyoni Superterrane, (MMST); Dodoma Basement Superterrane (DBST); Dodoma Schist Superterrane (DSST); Eastern Ubendian-Mtera Superterrane (EUMST); Kalenge-Burigi (KBST; not shown); Tectonic Front (TF; not shown); Mbulu-Masai Superterrane (MAST); Kilindi-Handeni Superterrane (KHST); Usagara-Ukaguru Superterrane (UKST); Uluguru-Pare Superterrane (UPST); Kabete et al., 2012a, b]. Although portions of this proposed tectonic framework require validation, the proposed model provides a potential explanation for the heterogeneous gold endowment within the Tanzanian Craton (for more details see Kabete et al., 2012a, b).

The newly defined tectonic subdivisions also provide a paradigm with which to explain the extension of gold-enriched superterranes into the metamorphic belts surrounding the Tanzanian Craton (Kabete et al., 2012a). To the east, the Tanzanian Craton is mantled by the Neoproterozoic-Palaeozoic East African Orogen (850–550 Ma, including the 650–620 Ma and ca. 550 Ma Mozambique Belt; e.g., Sommer et al., 2005a; Fritz et al., 2005; Thomas et al., 2013). The southern and western Tanzanian cratonic margins are bordered by the Palaeoproterozoic Usagaran and Ubendian Belts, respectively (2.1–1.8 Ga; e.g., Lenoir et al., 1994; Möller et al., 1998; Reddy et al., 2003; Boniface et al., 2012; Boniface and Schenk 2012). Finally, the northwestern margin of the Tanzanian Craton is bordered by the Mesoproterozoic Karagwe-Ankole Belt (ca. 1375 Ma; formally known as the Kibaran Belt; see De Waele et al., 2003, 2006, 2009; Tack et al., 2010 and Fernandez-Alonso et al., 2012 for recent discussions). In reality, each metamorphic belt is likely poly-orogenic and comprises, in part, reworked Archaean-Proterozoic crust. The details of this complex tectonic evolution is only beginning to emerge and only the Ubendian Belt, which hosts the Lupa Goldfield, is discussed in detail below.

2.2 Ubendian Belt

The Palaeoproterozoic Ubendian Belt is over 600 km long and ca. 150 km wide and comprises granulite-greenschist facies igneous and sedimentary rocks enveloping the western margin of the Tanzanian Craton. The NW-SE trending Ubendian Belt extends into northern

Malawi and Zambia and separates the Tanzanian and Congo Cratons. The belt is divided into eight litho-tectonic terranes (Katuma, Ikulu, Ubende, Wakole, Ufipa, Nyika, Upangwa, and Lupa; Daly, 1988) that are each separated by prominent NW-SE trending and steeply dipping shear zones (Fig. 2). The Palaeoproterozoic tectonic evolution of the belt is divided into two temporally distinct tectonic phases (Lenoir et al., 1994). The earliest of these tectonic phases, the 2.1–2.0 Ga Palaeoproterozoic Ubendian tectonic phase, is characterized by rare granulite facies tectonites and is considered to record the initial collision between the Tanzanian and Congo Cratons (Lenoir et al., 1994). This early Ubendian tectonic phase is overprinted by the second and younger 1.9–1.8 Ga Ubendian tectonic phase that resulted in the characteristic amphibolite-greenschist facies metamorphism and the NW-SE trending terrane-bounding shear zones (Lenoir et al., 1994). However, more recent work has identified disparately younger Mesoproterozic (ca. 1.09 Ga; Boniface et al., 2012) and Neoproterozoic-Palaeozoic (593–524 Ma; Boniface and Schenk, 2012) metamorphic events potentially related to the Irumide (1.05–1.00 Ga; De Waele et al., 2009) and Pan-African Orogens (950–450 Ma; Kröner, 1984; Stern, 1994). Neoproterozoic-Palaeozoic eclogite facies rocks dated at ca. 593, 548, 523 Ma provide particularly compelling evidence for disparately younger and previously unrecognized paleo-sutures within the Palaeoproterozoic Ubendian Belt (Boniface and Schenk, 2012). Together the available ages suggest that the Ubendian Belt is the product of at least three temporally discrete orogenic episodes. Moreover, later rifting associated with the western branch of the East African Rift, also likely contributed to the current geometry of the Ubendian Belt (Theunissen et al., 1996). The metallogenic implications of these overprinting metamorphic events are discussed further below.

2.0 Local Geology

2.1 Geology of Lupa Goldfield

The field area for the current study is located in the western portion of the Lupa Goldfield, SW Tanzania (Figs. 1−3). Previously reported U-Pb and Re-Os ages are summarized in Fig. 4 and Table 1. Foliated Archaean granites (2.76–2.72 Ga) are cut by non-foliated Palaeoproterozoic granites and dioritic-gabbroic intrusions (1.96–1.88 Ga; Lawley et al., 2013). Archaean granites are generally coarse grained, equigranular to porphyritic (K feldspar phenocrysts) and represent a range of modal mineralogy (syeno- to monzogranite) and compositions (Lawley et al., 2013). Primary Fe-Mg minerals have been variably replaced to a chlorite ± epidote ± muscovite ± calcite ± titanite ± magnetite mineral assemblage.

The oldest tectonic fabric (D1), which is the focus of this study, is largely restricted to these Archaean granites and is characterized by alternating quartzofeldspathic and chloritic folia that locally gives the granites a “gneiss-like” appearance (see legend of Fig. 3; Kimambo, 1984). The compositional banding is generally steeply dipping and varies in strike from E-W to NW-SE, but the fabric orientation and intensity can vary remarkably at the scale of individual outcrops. Cross cutting and overprinting relationships observed in drill core and outcrops imply that the D1 fabric, at least locally, preceded the emplacement of Palaeoproterozoic and non-foliated intrusions (i.e., D1 is locally ≥1.96 Ga). However, exposures of the Ilunga Syenogranite (ca. 1.96 Ga) at the Dubwana exploration target (Fig. 4) locally exhibit compositional banding (i.e., alternating quartzofeldspathic and chloritic folia) akin to the D1 fabric observed in Archaean granites and may suggest that D1 occurred diachronously during Palaeoproterozoic magmatism (discussed further below).

We expect that the D1 foliation developed at greenschist facies metamorphic conditions based on the chlorite ± muscovite ± epidote ± calcite metamorphic mineral assemblage and the dominant deformation microstructures (e.g., undulose extinction of quartz; crystal plastic deformation of quartz; Lawley et al., in press-b), which are typical of mid-crustal levels (300–450ºC; 1–3 kbar; Scholz, 1988). However, these inferred P-T conditions are notably lower than the amphibolite facies metamorphism that characterizes the other Ubendian Terranes and contrast with the “Acid Gneiss and Schist” lithologies that are reported to constitute large swaths of the Lupa Goldfield (Fig. 3; Kimambo, 1984). The field area for the current study (Fig. 4) is also devoid of ‘acid volcanic rocks’ and we suggest that the Lupa Goldfield geology map should be treated with caution (Fig. 3).

Palaeoproterozoic granitic-gabbroic intrusions in the Lupa Goldfield represent part of a voluminous magmatic arc at the Tanzanian cratonic margin (Figs. 2–4; see Manya, 2011 for further details). Two of these granites, the Saza Granodiorite and the Ilunga Syenogranite, are regionally extensive and are exposed across large tracts of the Lupa Goldfield and the field area for the current study (Figs. 3, 4). The Ilunga syenogranite (1960 ± 1 Ma; Lawley et al., 2013) is exposed in the northern portion of the field area and consists of a coarse grained and equigranular mineral assemblage of K feldspar ± quartz ± plagioclase with lesser amount of chloritized biotite. In contrast, the Saza Granodiorite (1935 ± 1 Ma; Lawley et al., 2013) is exposed in the southern portion of the field area and is characterized by a coarse grained and equigranular mineral assemblage of plagioclase ± quartz ± K feldspar with lesser amounts of chloritized hornblende ± biotite. Both granitoids possess dioritic-gabbroic enclaves and are also cut by dioritic-gabbroic dikes, which together suggest that intermediate-mafic magmatism pre- and post-dated the granitic intrusions. All magmatic phases in the field area have experienced greenschist facies metamorphism and are cut by D2 brittle-ductile and mylonitic shear zones (discussed further below). Later brittle faults cutting mineralized structures (D3) and faults filled with unconsolidated gouge likely record younger, but undated deformation event(s) that may be related to periodic reactivation of Palaeoproterozoic structures to the present day (Theunissen et al., 1996).

2.2 Gold Deposit Geology

Most of the exposed gold deposits and prospects are hosted by steeply south-dipping D2 quartz veins and greenschist facies mylonitic shear zones (Figs. 4, 6a–c). The majority of these are associated with the ENE-WSW trending Saza shear zone and two other dominant structural trends (NW-SE and E-W; Fig. 4). The Kenge and Mbenge deposits, which are broadly representative of the majority of prospects studied, contain a measured and indicated resource of 8.7 Mt at 1.33 g/t gold with a 0.5 g/t cut-off resulting in an estimated 0.37 Moz of contained gold (Simpson, 2012). The deposits are hosted, in part, by mylonitic shear zones cutting foliated Archaean granite (e.g., Fig. 6a). Hydrothermal alteration, strain and mineralization at these deposits are largely restricted to the host shear zone and associated laminated-quartz (± carbonate) veins (Fig. 6c), whereas quartz veins outside of the main shear zone represent a relatively minor contribution to the overall mineral resource.

Recent drilling by Helio Resource Corp. has identified a second, geologically distinct, style of mineralization (e.g., Porcupine) that comprises a moderately to steeply dipping panel of narrow and discontinuous mylonitic shear zones separated by non-foliated, but hydrothermally altered (sericitized and silicified) and veined granite (Fig. 6d, e). The Porcupine deposit contains a measured and indicated resource of 15.4 Mt at 1.31 g/t gold with a 0.5 g/t cut-off for an estimated 0.65 Moz of contained gold (Simpson, 2012). The highest gold grades (e.g., up to 40 g/t Au) at Porcupine are associated with shallow dipping quartz veins and intervals of sericitized, silicified and non-foliated Ilunga syenogranite (Fig. 6d, e). These auriferous and shallow dipping quartz veins primarily occur within the moderately to steeply dipping panel of hydrothermally altered granite and significantly widen the mineralized zone at Porcupine, but are notably absent at Kenge and Mbenge. Regardless of the deposit style, gold is associated with a relatively simple sulphide mineral assemblage of pyrite ± chalcopyrite ± molybdenite ± galena ± sphalerite.

2.3 Timing of Gold Mineralization

Five gold deposits and prospects were sampled for Re-Os geochronology (Fig. 4; Lawley et al., in press-a). Individual Re-Os molybdenite, pyrite and chalcopyrite model ages range from 1.95–1.88 Ga and are thus broadly contemporaneous with the entire 1.96–1.88 Ga magmatic history and the 1.9–1.8 Ga Ubendian tectonic phase (Fig. 5; Table 1). The absolute timing of gold within this temporal framework remains equivocal since gold is preferentially concentrated along pyrite crystal boundaries and locally occurs as pyrite fracture fills. These paragenetic relationships may provide evidence for a relatively late, and undated, gold event (Lawley et al., in press-a). Nevertheless, gold is observed as inclusions within ca. 1.88 Ga pyrite hosted by the main greenschist facies mylonitic shear zone at Kenge. This proposed ca. 1.88 Ga event is also recorded at all four of the other dated prospects (Mbenge, Porcupine, Konokono, and Dubwana). The paragenetic relationship between gold and these ca. 1.88 Ga pyrite and/or chalcopyrite samples at the other dated prospects is less clear, but the majority of samples were chosen from mineralized intervals and we suggest that the broad overlap of Re-Os sulphide ages between deposits and across the study area argues for a regional metallogenic event at ca. 1.88 Ga.

Disparately older ca. 1.95 and 1.94 Ga Re-Os molybdenite and pyrite model ages at Kenge were sampled from laminated and auriferous quartz veins hosted within the main mylonitic shear zone. The paragenetic relationship between gold and these sulphide samples is unclear and it remains equivocal whether: 1) the ca. 1.88 Ga gold event merely represents the youngest metallogenic event within a protracted (1.95–1.88 Ga) hydrothermal and progressive deformation history; or 2) the anomalously older Re-Os ages provide evidence for a telescoped deposit whereby the gold event at ca. 1.88 Ga merely overprints earlier, but unrelated style(s) of mineralization. Unfortunately the available ages and the ambiguous gold paragenesis do not allow us to rule out either of these possibilities. Nonetheless, the range of Re-Os ages suggest that laminated quartz veins possess protracted hydrothermal histories characterized by overprinting sulphidation events and that hydrothermal activity, at least locally, preceded the development of D2 mylonitic shear zones (Lawley et al., in press-a).

3.0 U-Pb titanite ID-TIMS Geochronology

3.1 Sample selection

Foliated Archaean granites, such as the one selected for this study (sample CL109; U-Pb zircon La-ICP-MS weighted average $^{207}Pb/^{206}Pb$ age 2757 ± 10 Ma; Table 1; Lawley et al., 2013), are characterized by alternating quartzofeldspathic and chlorite-rich folia that developed during D1. Titanite crystals are concentrated within the D1 chlorite-rich folia and the greenschist facies metamorphic assemblage of chlorite ± epidote ± calcite ± titanite overprinting the protolith’s Fe-Mg minerals (Figs. 7a, c). The petrographic association of titanite with the tectonic fabric and metamorphic mineral assemblage is consistent with titanite neo-crystallization during greenschist facies metamorphism (Essex and Gromet, 2000; Frost et al., 2001; Parrish, 2001). This mineral association is particularly apparent for the least-deformed examples of Archaean granites where mineral dissolution and volume loss is unlikely to explain the apparent concentration of metamorphic minerals. Moreover, euhedral titanite crystals isolated from the metamorphic mineral assemblage were not observed and suggests that any igneous titanite, which would be expected given the granitic composition, may have been recrystallized during subsequent metamorphism. The nature of the metamorphic phase transition is unclear, but could be related to the breakdown of primary clinopyroxene and/or amphibole by the hydration reaction clinopyroxene + ilmenite + quartz + H_2O = amphibole + titanite and/or the oxidation reaction amphibole + ilmenite + O_2 = titanite + magnetite + quartz + H_2O (Harlov et al., 2006). Metamorphic reactions such as these are postulated to play an important role during metamorphic titanite crystallization at greenschist facies P-T conditions (Frost et al., 2001).

Primary Fe-Mg minerals of the non-foliated Palaeoproterozoic Saza Granodiorite (sample CL1035; U-Pb zircon ID-TIMS weighted average $^{207}Pb/^{206}Pb$ age at 1935 ± 1 Ma; Lawley et al., 2013) are also replaced to a greenschist facies metamorphic mineral assemblage of chlorite ± epidote ± calcite ± titanite. The association of titanite with this metamorphic mineral assemblage is also consistent with titanite neo-crystallization during greenschist facies metamorphism, however euhedral titanite crystals isolated from the metamorphic mineral assemblage may represent relict magmatic titanite (Fig. 7d). Multiple titanite populations are characteristic of metamorphosed lithologies and are typically distinguished through a combination of optical/chemical characteristics and/or comparison of titanite ages with independent estimates for the crystallization age of the sample (Jung and Hellebrand, 2007). In this contribution, we follow a similar approach and compare new U-Pb titanite ages with previously reported U-Pb zircon ages for the same samples.

The titanite crystals present within the bulk mineral separate from sample CL109 and CL1035 are translucent, range in colour from brown to clear, and are present as broken fragments and fine-grained wedge-shaped crystals. For sample CL109, clear and relatively fine grained titanite crystals devoid of inclusions were chosen (Fig. 7e); whereas relatively much larger clear-brown titanite crystals devoid of inclusions from sample CL1035 were selected for U-Pb ID-TIMS analysis (Figs. 7f). The significance of these visually distinct titanite fractions is discussed further below.

3.2 Sample Preparation and ID-TIMS Methodology

All of the analysed titanite crystals were ultrasonically cleaned for an hour before being placed on a hotplate for 30 minutes, photographed in transmitted light and rinsed in ultrapure acetone. After rinsing, titanite fractions were transferred to 300 μl Teflon FEP microcapsules and spiked with a mixed ^{233}U–^{235}U–^{205}Pb tracer. Titanite crystals were then dissolved in ~120 μl of 29 M HF with a trace amount of 30% HNO_3 within microcapsules, placed in Parr vessels at ~220°C for 48 hours, dried to fluorides and then converted to chlorides at ~180°C overnight. U and Pb for all titanite fractions were separated using standard HBr and HNO_3-based anion-exchange chromatographic procedures. Isotope ratios were measured at the NERC Isotope Geosciences Laboratory (NIGL), UK, using a Thermo-Electron Triton Thermal Ionisation Mass-Spectrometer (TIMS). Pb and U were loaded separately on a single Re filaments in a silica-gel/phosphoric acid mixture. Pb was measured by peak hopping on a single SEM detector. U isotopic measurements were made in static Faraday mode. Age calculations and uncertainty estimation (including U/Th disequilibrium) was based upon the algorithms of Schmitz and Schoene (2007) and Crowley et al. (2007), using the updated consensus value of $^{238}U/^{235}U = 137.818 \pm 0.045$ (Hiess et al., 2012) and the decay constant and its uncertainty of Jaffey et al. (1971).

4.0 U-Pb titanite ID-TIMS results and interpretation

4.1 Common lead correction

Titanite crystals can incorporate significant concentrations of common lead during crystallization, which must be corrected for in order to determine accurate U-Pb ages (e.g., Frost et al., 2001). In general, the available approaches to common lead correction can be divided into three broad categories: 1) measure the lead isotopic composition of co-genetic and low-U phases, such as feldspar, and assume this isotopic composition is equivalent to common Pb at the time of titanite crystallization; 2) apply lead isotopic evolution models, such as the two-stage lead evolution model of Stacey and Kramers (1975; S-K model), and assume that this composition is equivalent to the isotopic composition of common Pb at the time of titanite crystallization; and 3) utilize regression techniques, such as the 'Total Pb/U isochron', which requires no *a priori* assumption of the common lead's isotopic composition (Ludwig, 2008).

The analysis of low-U mineral phases (e.g., feldspar) was deemed inappropriate for our data set since titanite crystals occurs with the metamorphic mineral assemblage and is therefore unlikely to be in isotopic equilibrium with igneous feldspar. Furthermore, previous Pb isotopic studies have demonstrated complex Pb isotopic systematics of feldspar (and galena) for samples taken from the Ubendian and Usagaran Belts, which likely reflects metamorphic overprinting and open system behavior during multiple orogenic cycles at the Tanzanian cratonic margin (e.g., Möller et al., 1998). The 'Total Pb/U Isochron' (Ludwig, 1998; Ludwig, 2008) makes no *a priori* assumption as to the isotopic composition of common Pb and, providing the data set represents a suite of co-genetic and undisturbed titanite fractions that share a common Pb isotopic composition, represents a robust approach to common lead correction (e.g., Corfu and Stone, 1998; Storey et al., 2006). Unfortunately, titanite fractions from CL109 and CL0975 show evidence of disturbance to the U-Pb systematics (discussed further below) and so for the remaining discussion common lead for both samples was corrected by employing the S-K model approach. The sensitivity of the analyzed titanite fractions to the S-K model common lead correction is discussed further below.

4.2 U-Pb titanite ID-TIMS results and interpretation

4.2.1 Archaean Granite (CL109)

U-Pb titanite data are reported in Table 2 and Fig. 8. For the foliated Archaean granite (sample CL109), nine titanite fractions yield $^{238}U/^{204}Pb$ and $^{206}Pb/^{204}Pb$ ratios ranging from 110–545 and 40–190, respectively. Common lead is significant for this dataset as suggested by the low Pb^*/Pb_c ratios (1–9; where Pb^* and Pb_c correspond to radiogenic and common lead, respectively). As a result, the choice of the isotopic composition of common lead can have a substantial impact on the calculated U-Pb ages. We tested the effect of the assumed common lead composition on titanite ages by varying the S-K model age composition from 2.5–1.5 Ga and found that some individual $^{207}Pb/^{206}Pb$ titanite ages varied considerably, whereas the weighted average $^{207}Pb/^{206}Pb$ titanite age of all the analyzed titanite fractions did not (weighted average $^{207}Pb/^{206}Pb$ ages range from 1943–1911 Ma; Fig. 8a inset). Titanite fractions S3 and S4 are considerably more sensitive to the assumed common lead composition and also possess anomalously younger $^{207}Pb/^{206}Pb$ ages for S-K model Pb compositions at 1.5 and 1.9 Ga, whereas the other seven titanite fractions were relatively insensitive to the S-K model lead isotopic composition and possess $^{207}Pb/^{206}Pb$ ages that overlap within analytical uncertainty at the 2σ level (Fig. 8a inset). As a result, the common lead isotopic composition was assumed by selecting the S-K model lead isotopic composition at 1.9 Ga, which we use as a reasonable first order approximation of its true value.

A conventional 2D Terra-Wasserburg regression of the seven common Pb corrected and insensitive titanite fractions yield a Model 1 York regression solution upper intercept age of 1921 ± 7 Ma (MSWD = 0.7; probability of fit = 0.6; n = 7; Fig. 8a). It is important to note, that these

Palaeoproterozoic ages for titanite are all considerably younger than the LA-ICP-MS weighted average $^{207}Pb/^{206}Pb$ zircon age for the same sample (2757 ± 10 Ma; Fig. 8a; Lawley et al., 2013). The geological significance of these Palaeoproterozoic titanite ages is discussed further below.

4.2.2 Saza Granodiorite (CL0975)

The five titanite fractions analyzed from the Saza Granodiorite (sample CL0975) possess a range of $^{238}U/^{204}Pb$ and $^{206}Pb/^{204}Pb$ from 294–859 and 118–315, respectively. These ratios, and in particular the relatively higher Pb*/Pbc ratios (5–13), suggest that titanite crystals from CL0975 are more U rich and possess less common Pb than titanite analyses from CL109. We tested the effect of the assumed common Pb composition on titanite ages, as above, by varying the S-K model age composition from 2.5–1.5 Ga and found that individual $^{207}Pb/^{206}Pb$ titanite ages and weighted average $^{207}Pb/^{206}Pb$ titanite ages were both relatively insensitive to the inferred isotopic composition of common lead (weighted average $^{207}Pb/^{206}Pb$ ages range from 1942–1924 Ma; Fig. 8b inset). As above, the common lead isotopic composition was assumed by selecting the S-K model lead isotopic composition at 1.9 Ga, which we expect is the best first order approximation of its true value.

A conventional 2D Terra-Wasserburg regression of the five common Pb corrected titanite fractions yield a Model 1 York regression solution upper intercept age of 1931 ± 3 Ma (MSWD = 1.1; probability of fit = 0.4; n = 5; Fig. 8b). This upper intercept regression age is comparable to a weighted average $^{207}Pb/^{206}Pb$ age of the three concordant titanite fractions, which represent the least disturbed titanite fractions, at 1930 ± 3 Ma (MSWD = 0.6; probability of fit = 0.5; n = 3). Both the weighted average (based on the three concordant and thus least disturbed titanite fractions) age and the 2D regression age (based on all of the analyzed titanite fractions) ages are in excellent agreement with each other and are only slightly outside of analytical uncertainty at the 2σ level with a high-precision ID-TIMS weighted average $^{207}Pb/^{206}Pb$ zircon age of 1935 ± 1 Ma (Lawley et al., 2013) for the same sample (Fig. 8b).

5.0 Discussion

5.1 Geological significance of U-Pb titanite ages

5.1.1 Archaean Granite (CL109)

Titanite crystals from the foliated Archaean granite sample (CL109) are spatially associated with the metamorphic fabric/mineral assemblage and provide evidence for titanite neo-crystallization related to the breakdown of primary Fe-Mg minerals during greenschist facies metamorphism and the development of the D1 deformation fabric (Fig. 7). The generally low

Pb^*/Pb_c ratios (1–9; Table 2) of the analyzed titanite fractions support this interpretation and are consistent with the compositional characteristics (i.e., relatively high common lead and low U) of metamorphic titanite reported in previous studies (e.g., Frost et al., 2001; Jung and Hellebrand, 2007). Whilst the precise age of titanite fractions from CL109 remains open to interpretation due to, in part, the sensitivity of U-Pb ages to the assumed isotopic composition of common lead, these new U-Pb data clearly show that titanite crystals are in fact Palaeoproterozoic and therefore considerably younger than Archaean U-Pb zircon ages for the same sample (Fig. 8a; Table 1).

Sample CL109 is cut by a non-foliated gabbroic dyke that is dated by LA-ICP-MS U-Pb zircon geochronology at ca. 1.88 Ga (Lawley et al.,2013), which is consistent with the ca 1.92 Ga U-Pb titanite age interpreted to date the timing of D1. However, elsewhere foliated Archaean granites are cut by ca. 1.96 Ga granodioritic-granitic dykes and intrusions (most notably the 1960 ± 1 Ma Ilunga Syenogranite; Lawley et al., 2013), which is significantly older (ca. 40 Myr older than the upper Concordia intercept age at 1921 ± 7 Ma ; Fig. 8a) than the inferred D1 timing reported here. This suggests either: 1) D1 is more complex than previously thought and developed diachronously during Palaeoproterozoic magmatism (Fig. 9); and/or 2) that U-Pb titanite dates from sample CL109 are younger than their true age as a result of Pb-loss and/or inappropriate common Pb correction (Fig. 8b). The latter is supported by the absence of a ductile deformation fabric within the Saza Granodiorite (ca. 1.93 Ga), which would be expected if D1 had occurred at ca. 1.92 Ga (Fig. 9e). Alternatively, the D1 fabric may have developed episodically during the emplacement of Palaeoproterozoic granites, which is consistent with compositional banding akin to the D1 fabric observed in Archaean granites, but locally observed in the Ilunga Syenogranite at Dubwana.

The current data set does not allow us to rule out either of these possibilities and thus the precise timing of D1 deformation remains unclear. Nevertheless, these new U-Pb titanite ages provide new evidence to suggest that the earliest identifiable deformation event in the Lupa Goldfield occurred during the Palaeoproterozoic and some 40 Myr prior to D2 mylonitic shear zones and gold at ca. 1.88 Ga. This extended Palaeoproterozoic structural history places important new constraints on the onset of deformation related to Ubendian orogenesis and raises the possibility that fabric development during D1 may have played an important role in localizing strain during later deformation (see below for further discussion).

5.1.2 Saza Granodiorite (CL0975)

Titanite crystals from the non-foliated Saza granodiorite (sample CL0975) are locally associated with the greenschist facies mineral assemblage overprinting the Saza Granodiorite and thus exhibit textural similarities in thin section to titanite crystals extracted from the foliated Archaean granite (sample CL109). However, titanite crystals isolated from the Saza Granodiorite are visually distinct (i.e., larger and are brown-translucent), which suggests that these titanite crystals may represent a titanite population dissimilar to metamorphic titanite observed in sample CL109 (Figs. 7e, f). The higher $^{206}Pb/^{238}U$ ratios and generally higher Pb^{*}/Pb_{c} ratios (5–13; Table 2) within the analyzed titanite fractions from the Saza Granodiorite are also unlike titanite fractions from the foliated Archaean granite and are more consistent with the more radiogenic composition of magmatic titanite (e.g., Jung and Hellebrand, 2007).

The weighted average $^{207}Pb/^{206}Pb$ titanite age of the three concordant titanite analyses (1930 ± 3 Ma) are slightly outside of analytical uncertainty of the weighted average $^{207}Pb/^{206}Pb$ zircon age (1935 ± 1 Ma) of concordant zircons for the same sample and support a magmatic origin for the analyzed titanite fractions. The broad agreement between both geochronometers suggests that the Stacey and Kramers (1975) common lead correction approach is broadly appropriate despite two of the common lead corrected titanite fractions exhibiting severe reverse discordance (Fig. 8b). The cause of reverse discordance is unclear and could be related to U loss and/or represent an analytical effect. The slight discrepancy between the interpreted crystallization age and U-Pb titanite ages could be related to minor Pb-loss in the analyzed titanite fractions, later closure during cooling, sub-solidus recrystallization, and/or inadequate accounting for the common lead correction (Frost et al., 2001). If the nominally younger U-Pb titanite ages represent cooling ages, our results would suggest that the Saza Granodiorite cooled relatively quickly since U-Pb titanite and zircon ages are only <1 Myr outside of analytical uncertainty at the 2σ level.

5.2 Implications for ore deposit models

Here we integrate new U-Pb titanite ages with previously reported U-Pb and Re-Os ages to address some of the outstanding uncertainties (e.g., the temporal relationship between D1 and D2) at gold prospects within the Lupa Goldfield. At least three temporally distinct hydrothermal events have been identified in the Lupa Goldfield (1.95, 1.94 and 1.88 Ga; Lawley et al., in press-a; Fig. 5). Gold is expected to have been introduced at ca. 1.88 Ga, whereas the relationship between gold and disparately older Re-Os model ages at ca. 1.95 Ga and 1.94 Ga is less clear. Each of these broadly defined hydrothermal events are represented in detail by complex vein histories that suggest each event occurred at a time scale that is less than the resolution of the Re-Os method. This episodic, but protracted hydrothermal history (1.95–1.88 Ga) overlaps with the Palaeoproterozoic magmatic history of the Goldfield as determined by U-Pb zircon dating of felsic-mafic intrusions/dykes (1.96–1.88 Ga; Fig. 5). Furthermore, high-precision U-Pb zircon ID-TIMS ages for the Saza Granodiorite (1935 ± 1 Ma) overlap with Re-Os molybdenite ages (ca. 1.94 Ga) and provide unequivocal evidence for sulphidation that is concomitant with magmatism at the million-year time scale.

This close temporal relation has led to the suggestion that gold deposits within the Lupa Goldfield belong to the intrusion-related ore deposit type (Manya, 2012). However, Re-Os model ages pre- and post-date individual magmatic phases and hydrothermal activity appears to have occurred at a time scale that is far greater than the expected duration of a single magmatically derived hydrothermal fluid circulation system (e.g., <1 Myr; von Quadt et al., 2011). Moreover, the proposed gold event at ca. 1.88 Ga is disparately younger than any of the dated granites and we suggest that a simple intrusion-related deposit model (e.g., Manya, 2012) whereby metalliferous and hydrothermal fluids exsolving from the Saza Granodiorite are solely responsible for gold is unsupported.

New U-Pb titanite ages reported here further constrain ore deposit models by demonstrating that the onset of deformation occurred during the Palaeoproterozoic. It further suggests that deformation was progressive and broadly overlaps with Palaeoproterozoic magmatism (Figs. 5, 9). The broad temporal overlap between hydrothermal (1.95–1.88 Ga), magmatic (1.96–1.88 Ga) and deformation (≥1.92–1.88 Ga) events in the Lupa Goldfield are also well correlated to the tectono-thermal history recorded by the other Ubendian Terranes (i.e., the 2.1–1.8 Ga Ubendian Orogeny and specifically the 1.9–1.8 Ga Ubendian tectonic phase; Lenoir et al., 1994). In particular, the Palaeoproterozoic MORB-like chemistry eclogites (ca. 1.89 and 1.86 Ga; Boniface et al., 2012) sampled from the Ubende Terrane demonstrates that high-grade metamorphism related to subduction of oceanic crust broadly overlaps with the proposed gold event at ca. 1.88 Ga within the Lupa Goldfield. Palaeoproterozoic eclogitic rocks in the Ubende Terrane are amongst the oldest eclogites on Earth (Boniface et al., 2012) and therefore represent a key link between metallogenesis related to modern and ancient subduction zone processes. A holistic understanding of Ubendian tectonics requires additional constraints on the significance and distribution of Meso- and Neoproterozoic metamorphic overprints. Nevertheless, the link between Palaeoproterozoic convergent tectonics, subduction zone processes and gold mineralization in the Lupa Goldfield is implied.

The consistent sulphide mineralogy between gold prospects, in conjunction with a comparable alteration mineral assemblage and overlapping sulphide ages, suggests that all of the studied gold prospects are consanguineous and can be considered as part of the same broad mineralization history related to an interconnected shear zone network that focused fluids at the

Tanzanian cratonic margin during Palaeoproterozoic Ubendian orogenesis. Together the timing, structural setting and geological characteristics suggest that gold prospects exposed in artisanal workings within the western Lupa Goldfield are typical of the orogenic gold deposit type [i.e., shear and quartz-carbonate vein hosted, sulphide poor and Au dominated deposits that result from structural focusing of low salinity H_2O-CO_2 ($\pm$ CH_4) fluids at convergent margins; *sensu* Groves et al., 1998]. Our ages are also consistent with other palaeo-convergent margins where systematic geochronology has demonstrated that orogenic style gold mineralization can occur throughout orogenesis, but generally occurs relatively late during the orogen's tectono-thermal history (e.g., Sarma et al., 2011; Figs. 5, 9f).

5.3 Archaean versus Proterozoic Tanzanian Gold Deposits

In the preceding section we argue that gold deposits in the Lupa Goldfield share similarities to the orogenic gold deposit type. In this section we compare and contrast the geology of goldfields hosted within and at the margins of the Tanzanian Craton. The geologic characteristics of deposits within each goldfield are taken from the available literature and are summarized in Table 3. Overall, gold deposits within the Lake Victoria Goldfield share a number of broad similarities with Palaeoproterozoic (e.g., ca. 1.88 Ga, Lupa), Mesoproterozoic (e.g., ca. 1.2 Ga, Mpanda; Kazimoto and Schenk, 2013), and Palaeozoic (e.g., ca. 483 Ma, Niassa; Bjerkgard et al., 2009) goldfields situated within metamorphic belts marginal to the Tanzanian Craton (Fig. 1). These gross geologic similarities include comparable hydrothermal alteration mineral assemblages (sericite, chlorite, silica flooding, carbonate), sulphide mineral assemblages (pyrite ± base-metal sulphides), metamorphic grade (amphibolite to greenschist) and similar apparent controls on gold mineralization (predominately shear- and quartz vein-controlled and lithologic contacts). However, in detail each deposit also possesses distinct geologic characteristics that make direct comparisons between deposits — even within a single goldfield — challenging. For example, the BIF-hosted Geita and intrusion-hosted Buzwagi deposits differ from the other meta-sedimentary and –volcanic rocks hosted deposits in the Lake Victoria Goldfield (Table 3).

Nevertheless goldfield comparisons such as those presented in Table 3 represent an important exercise since several of the metamorphic belts enveloping that Tanzanian Craton are now recognized to comprise, in part, re-worked Archaean crust (Ubendian Belt, Kazimoto and Schenk, 2013, Lawley et al., 2013; Usagaran, Sommer et al., 2005b; Mozambique Belt, Kröner et al., 2003; Sommer et al., 2005a; Thomas et al., 2013). As a result, these metamorphic belts may host Archaean gold deposits that have been subsequently re-worked during Palaeoproterozoic-

Palaeozoic orogenic episodes. Unequivocal examples of re-worked Archean deposits have not been documented in Tanzania, but represent hitherto unrecognized gold potential within Proterozoic-Palaeozoic metamorphic belts surrounding the Tanzanian Craton (Kabete et. al., 2012a). Moreover, orogenic gold deposits hosted by re-worked Archaean crust are scarce globally although the Mesozoic goldfields within the North China Craton may represent possible exceptions (Li et al., 2012).

Gold deposits within the Lupa goldfield provide other natural examples of this unusual deposit setting since the inferred ca. 1.88 Ga gold event is hosted, in part, by re-worked Archaean granitoids. Individual Mesoproterozoic Re-Os ages at ca. 1371 Ma and 1057−922 Ma (Lawley et al., in press-a) and inferred lead-loss events at 514−469 Ma (Lawley et al., 2013), although not directly related to gold in the Lupa goldfield, are potentially related to later overprinting during multiple and temporally-discrete orogenic cycles (ca. 1375 Ma, Karagwe-Ankole Belt; 1.05–1.00 Ga Irumide Orogeny; 950–450 Ma Pan African Orogeny). Preliminary U-Pb monazite ages at ca. 1.2 Ga provide evidence for a potential Mesoproterozoic gold event at the Mpanda goldfield, which is also hosted, in part, by Archaean rocks re-worked during Palaeo- and Mesoproterozoic tectono-thermal events (Kazimoto and Schenk, 2013). However, the precise age of the Mpanda goldfield remains unclear because previously reported Pb-Pb model ages provided evidence for a disparately younger gold event at ca. 720 Ma (Stendal et al., 2004). Neoarchean-Palaeozoic gold is also reported in the ca. 743 Ma Niassa Goldfield, which are interpreted to reflect Pan-African orogenic style gold mineralization in NW Mozambique (Bjerkgard et al., 2009). Similar Pan-African gold events are also reported in other countries bordering the Tanzanian Craton although the geologic setting of these deposits remains poorly understood (Burundi, Rwanada, Uganda; Brinckmann et al., 1994; Fernandez-Alonso et al., 2012).

The examples provided above suggest that the metamorphic belts bordering the Tanzanian Craton are prospective for orogenic style gold mineralization spanning at least three orogenic episodes. The available geochronologic database highlights the importance of robust geochronometers that remain closed during overprinting geologic events. It also stresses the need for robust geochronometers that record and, can be paragenetically linked to, different stages of the tectono-thermal history. The latter is particularly important in poly-orogenic settings where the enrichment or possible remobilization of gold through time is expected to be a key process for gold deposits hosted by metamorphic belts (Groves et al., 2003).

5.4 Structural evolution of the Lupa Goldfield

New U-Pb titanite ages from an Archaean granite sample (CL109) demonstrates the onset of deformation in the Lupa Goldfield occurred during the Palaeoproterozoic and pre-dated D2 auriferous mylonites by ≥40 Myr. Here we suggest that foliated Archaean granites, developed during D1, acted as zones of pre-existing structural weakness and/or heterogeneity and may have played a key role in strain localization during later deformation. This is particularly apparent for gold prospects hosted by D2 mylonitic shear zones developed within foliated Archaean granites such as at Kenge and Mbenge (Fig. 6a). At these mineral systems, the orientation of mylonitic shear zones closely follows the geometry of the D1 fabric (Lawley et al., in press-b). The sharp contacts between the mylonitic shear zones and foliated wall rock suggests that the D1 fabric was not passively re-oriented during subsequent deformation, and instead suggests D1 fabric acted as a structural weakness and/or heterogeneity that localized strain during D2 (e.g., Fig. 6b). However for several shear zones (e.g., Saza shear zone), and for those gold prospects hosted by non-foliated Palaeoproterozoic intrusive phases, the importance of D1 deformation on the development of auriferous shear zones is unclear.

Re-Os dating has also identified hydrothermal events (ca. 1.95 and 1.94 Ga; Lawley et al., in press-a) that pre-date the timing of D1 reported as part of this study (ca. 1.92 Ga). These anomalously older sulphides were sampled from laminated quartz veins filling and deformed by D2 mylonitic shear zones at Kenge. The latter suggests that quartz veining may have in fact, at least locally, pre-dated the D1 fabric (Fig. 9d). Unfortunately, the uncertainty in the common-lead correction precludes a precise U-Pb titanite age for the onset of ductile deformation and does not allow us to evaluate this possibility further. Nevertheless, structural preparation has been shown to play an important role at goldfields where orogenic style gold mineralization is kinematically late (Groves et al., 2000). Pre-existing structures, such as brittle faults and/or lithologic contacts, are widely recognized as 'stress risers' that facilitate reactivation over the formation of new structures at the deposit scale (e.g., Dubé et al., 1989; Lin and Corfu, 2002).

The importance of structural reactivation is also suggested by the link between orogenic gold style mineralization, compressional to transpressional settings and "mis-oriented" high-angle reverse shear zones (e.g., Sibson, 1988). In these geologic settings and in a compressional stress regime, high-angle reverse faults are more likely to represent reactivation of pre-existing structures due to high fluid pressure and/or low frictional fault strength rather than newly developed structures (Lawley et al., in press-b). We suggest that D1 and, particularly the development of planes comprising rheologically weak chloritic folia, created zones of structural weakness that may have, at least locally, acted as pre-existing anisotropies that were potentially reactivated during later D2 brittle-ductile deformation. The abundance of chlorite slickensides on

D1 chloritic folia, which are unlikely to have formed during the dominantly ductile D1 event(s), supports this interpretation and also suggests that early ductile deformation may have been reactivated during late brittle faulting (D3).

Together the available field relationships and absolute ages of deformation fabrics record a broad progression from dominantly D1 ductile (ca. 1.92), to D2 brittle-ductile auriferous mylonitic shear zones and quartz veins (ca. 1.88 Ga) and ultimately to D3 cataclasites and discrete faults during later, but undated, and dominantly brittle deformation. A similar progression in deformation characteristics, i.e. from dominantly ductile to brittle deformation, has also been reported in goldfields associated with more modern orogenic settings and has been attributed to changing P-T conditions during orogenic uplift, denudation and cooling (e.g., Alps; Pettke et al., 1999).

6.0 Conclusions

Titanite U-Pb geochronology for a foliated Archaean granite, which represents the earliest identifiable deformation event in the Lupa Goldfield, suggests that the onset of deformation occurred during the Palaeoproterozoic at ca. 1.92 Ga. This age raises new questions regarding the timing of the D1 fabric and suggests either: 1) titanite dates are slightly younger than their true age due to lead-loss or an inaccurate common lead correction; and/or 2) that D1 is more complex than previously recognized and occurred diachronously during the emplacement of Palaeoproterozoic intrusions. New U-Pb titanite ages for the non-foliated Saza Granodiorite at 1930 ± 3 Ma, are only nominally younger than the U-Pb zircon age (1935 ± 1 Ma) for the same sample.

These U-Pb titanite ages, combined with previously reported U-Pb zircon and Re-Os sulphide geochronology, constrain the Palaeoproterozoic timing of magmatism (1.96–1.88 Ga), hydrothermal activity (1.95–1.88 Ga) and deformation/metamorphism (≥1.92–1.88 Ga) in the Lupa Goldfield. Together the available geochronologic data demonstrate a progression from dominantly ductile (D1) to brittle-ductile deformation (D2) over ≥40 Myr, which occurred diachronously and intermittent with felsic-mafic plutonism during a Palaeoproterozoic orogenic cycle at the Tanzanian cratonic margin. However, the inferred ca. 1.88 Ga gold event in the Lupa Goldfield simply represents the earliest episode of orogenic gold deposit formation in western Tanzania and are superseded by younger orogenic gold style mineralization events related to temporally discrete orogenic episodes at cratonic margins bordering the Ubendian Belt. The Tanzanian cratonic margin is therefore highly prospective for orogenic style gold mineralization, which may have developed during multiple orogenic events.

Acknowledgements

CJML would like to thank funding provided by a Durham Doctoral Fellowship and a student research grant awarded by the Society of Economic Geologists. Helio Reosurce Corp. also provided funding, logistical support and access to the exploration licenses for sampling. The manuscript benefitted from critical reviews by Nicole Rayner, Richard Goldfarb and Joas Kabete. Emmanuel Kazimoto also improved the manuscript by providing additional details concerning the geology of the Mpanda and Lake Victoria Goldfields. Natural Resources Canada Earth Science Sector contribution No. 20130046.

References

AngloGold Ashanti Annual Report, 2012, www.anglogold.com, 125 p.

Arne, D.C., Bierlein, F.P., Morgan, W., Stein, H.J., 2001. Re-Os dating of sulfides associated with gold mineralization in central Victoria, Australia. Economic Geology, 96, 1455–1459.

Barrick Gold Corporation Annual Report 2012, www.africabarrickgold.com, 180 p.

Bell, K., Dodson, M.H., 1981. The geochronology of the Tanzanian Shield. The Journal of Geology, 89, 109−128.

Bierlein, F.P., Groves, D.I., Cawood, P.A., 2009. Metallogeny of accretionary orogens – the connection between lithospheric processes and metal endowment. Ore Geology Reviews, 36, 282–292.

Bjerkgard, R., Stein, H.J., Bingen, B., Henderson, I.H.C., Sandstad, J.C., Moniz, A., 2009. The Niassa Gold Belt, northern Mozambique – a segment of a continental-scale Pan-African gold-bearing structure? Journal of African Earth Sciences, 53, 45–58.

Boniface, N., Schenk, V., Appel, P., 2012. Paleoproterozoic eclogites of MORB-type chemistry and three Proterozoic orogenic cycles in the Ubendian Belt (Tanzania): Evidence from monazite and zircon geochronology, and geochemistry. Precambrian Research, 192–195, 16–33.

Boniface, N., Schenk, V., 2012. Neoproterozoic eclogites in the Paleoproterozoic Ubendian Belt of Tanzania: Evidence for a Pan-African suture between the Bangweulu Block and the Tanzania Craton. Precambrian Research, 208–211, 72–89.

Borg, G., Shackleton, R.M., 1997. The Tanzania and NE Zaire Cratons, In: Wit, M.J., Ashwal, L.D., (Eds.), Greenstone Belts. Clarendon Press, Oxford, p. 608–619.

Borg, G., Krogh, T., 1999. Isotopic age date of single zircons from the Archaean Sukumaland Greenstone Belt, Tanzania. Journal of African Earth Sciences, 29, 301–312.

Botcharnikov, R.E., Linnen, R.L., Wilke, M., Holtz, F., Jugo, P.J., Berndt, J., 2011. High gold concentrations in sulphide-bearing magma under oxidizing conditions. Nature Geoscience, 4, 112–115.

Brinckmann, J., Lehmann, B., Timm, F., 1994. Proterozoic gold mineralization in NW Burundi. Ore Geology Reviews, 9, 85−103.

Brown, T.J., Shaw, R.A., Bide, T., Petavratzi, E., Raycraft, E.R., Walters, A.S., 2013. World Mineral Production 2007−11, British Geological Survey, Keyworth, Nottingham, 85 p.

Bucci, L.A., McNaughton, N.J., Fletcher, I.R., Groves, D.I., Kositcin, N., Stein, H.J., Hagemann, S.G., 2004. Timing and duration of high-temperature gold mineralization and spatially associated granitoid magmatism at Chalice, Yilgarn Craton, Western Australia. Economic Geology, 99, 1123–1144.

Cahen, L., Snelling, N.J., Delhal, J., Vail, J., 1984. The Geochronology and Evolution of Africa, Clarendon Press, Oxford, 512 p.

Chamberlain, C.M., 2003. Geology and genesis of the Bulyanhulu gold deposit, Sukumaland greenstone belt. Unpublished PhD Thesis, Imperial College London, London.

Corfu, F., Stone, D., 1998. The significance of titanite and apatite U-Pb ages: Constraints for the post-magmatic thermal-hydrothermal evolution of a batholithic complex, Berens River area, northwestern Superior Province, Canada. Geochimica et Cosmochimica Acta, 62, 2979–2995.

Crowley, J.L., Schoene, B., Bowring, S.A., 2007. U-Pb dating of zircon in the Bishop Tuff at the millennial scale: Geology, 35, 1123–1126

Clifford, T.N., 1970. The structural framework of Africa, In: Clifford, T.N., and Gass, I., (Eds.), African Magmatism and Tectonics. Oliver and Boyd, Edinburgh, 1–26.

Cloutier, J., Stevenson, R.K., Bardoux, M., 2005. Nd isotopic, petrological and geochemical investigation of the Tulawaka East gold deposit, Tanzanian Craton. Precambrian Research, 139, 147−163.

Daly, M.C., 1988. Crustal shear zones in central Africa; a kinematic approach to Proterozoic tectonics. Episodes, 11, 5–11.

Davis, D.W., Lin, S.F., 2003. Unraveling the geologic history of the Hemlo Archean gold deposit, Superior province, Canada: a U-Pb geochronological study. Economic Geology, 98, p. 51–67.

De Waele, Wingate, M.T.D., Fitzsimons, Mapani, B.S.WE., 2003. Untying the Kibaran knot: A reassessment of Mesoproterozoic correlations in southern Africa based on SHRIMP U-Pb data from the Irumide belt. Geology, 31, 509–512.

De Waele, B., Kampunzu, A.B., Mapani, B.S.E., Tembo, F., 2006. The Mesoproterozoic Irumide belt of Zambia. Journal of African Earth Sciences, 46, 36–70.

De Waele, B., Fitzsimons, I.C.W., Wingate, M.T.D., Tembo, F., Mapani, B., 2009. The geochronological framework of the Irumide Belt of Zambia: A prolonged crustal history along the margin of the Bangweulu Craton. American Journal of Science, 309, 132–187.

Dubé, B., Poulsen, K.H., Guha, J., 1989. The effects of layer anisotropy on auriferous shear zones: the Norbeau Mine, Quebec. Economic Geology, 84, 871–878.

Dziggel, A., Poujol, M., Otto, A., Kisters, A.F.M., Trieloff, M., Schwarz, W.H., Meyer, F.M., 2010. New U-Pb and Ar-40/Ar-39 ages from the northern margin of the Barberton greenstone belt, South Africa: Implication for the formation of Mesoarchaean gold deposits. Precambrian Research, 179, 206–220.

Essex, R., Gromet, L.P., 2000. U-Pb dating of prograde and retrograde titanite growth during the Scandian orogeny. Geology, 28, 419–422.

Fernandez-Alonso, M., Cutten, H., De Waele, B., Tack, L., Tahon, A., Baudet, D., Barritt, S.D., 2012. The Mesoproterozoic Karagwe-Ankole Belt (formerly the NE Kibara Belt): The result of prolonged extensional intracratonic basin development punctuated by two-short lived far-field compressional events. Precambrian Research, 216–219, 63–86.

Fritz, H., Tenczer, V., Hauzenberger, C.A., Wallbrecher, E., Hoinkes, G., Muhongo, S., Mogessie, A., 2005. Central Tanzanian tectonic map: A step forward to decipher Proterozoic structural events in the East African Orogen: Tectonics, 24, TC6013, 26 p.

Frost, B.R., Chamberlain, K.R., Schumacher, J.C., 2001. Sphene (titanite): phase relations and role as a geochronometers. Chemical Geology, 172, 131–148.

Fu, B., Kendrick, M.A., Fairmaid, A.M., Phillips, D., Wilson, C.J.L., Mernagh, T.P., 2012. New constraints on fluid sources in orogenic gold deposits, Victoria, Australia. Contributions to Mineralogy and Petrology, 163, 427–447.

Goldfarb, R.J., Groves, D.I., Gardoll, S., 2001. Orogenic gold and geologic time: A global synthesis. Ore Geology Reviews, 18, 1−75.

Groves, D.I., Goldfarb, R.J., Gebre-Mariam, M., Hagemann, S.G., Robert, F., 1998. Orogenic gold deposits: A proposed classification in the context of their crustal distribution and relationships to other gold deposit types. Ore Geology Reviews, 13, 7–27.

Groves, D.I., Goldfarb, R.J., Knox-Robinson, C.M., Ojala, J., Gardoll, S., Yun, G.Y., Holyland, P., 2000. Late-kinematic timing of orogenic gold deposits and significance for computerbased exploration techniques with emphasis on the Yilgarn Block, Western Australia. Ore Geology Reviews, 17, 1–38.

Groves, D.I., Goldfarb, R.J., Robert, F., Hart, C.J.R., 2003. Gold deposits in metamorphic belts: Overview of current understanding, outstanding problems, future research and exploration strategies. Economic Geology, 98, 1–29.

Harlov, D., Tropper, P., Seifert, W., Nijland, T., Forster, H.-J., 2006. Formation of Al-rich titanite ($CaTiSiO_4O$–$CaAlSiO_4OH$) reaction rims on ilmenite in metamorphic rocks as a function of fH_2O and fO_2. Lithos, 88, 72–84.

Hiess, J., Condon, D. J., McLean, N., Noble, S. R., 2012. $^{238}U/^{235}U$ systematics in terrestrial uranium-bearing minerals. Science, 335, 1610-1614.

Hronsky, J.M.A., Groves, D.I., Loucks, R.R., Begg, G.C., 2012. A unified model for gold mineralization in accretionary orogens and implications for regional-scale exploration targeting methods. Mineralium Deposita, 47, 339–358.

Ikingura, J.R., Akagi, H., Mujumba, J., Messo, C., 2006. Environmental assessment of mercury dispersion, transformation and bioavailability in the Lake Victoria Goldfields, Tanzania. Journal of Environmental Management, 81, 167−173.

Ikingura, J.R., Mutakyahwa, M.K.D., Marobhe, I.M., Manya, S., Kazimoto, E.O., Mshiu, E.E., Charles, K., 2009. Atlas of gold deposits in Tanzania, 1st ed. University of Dar es Salaam, Dar es Salaam, Tanzania.

Jaffey, A.H., Flynn, K.F., Glendenin, L.E., Bentley, W.C., Essling, A.M., 1971. Precision measurement of half-lives and specific activities of ^{235}U and ^{238}U. Physical Reviews C4, 4, 1889–1906.

Jung, S., Hellebrand, E., 2007. Textural, geochronological and chemical constraints from polygenetic titanite and monogenetic apatite from a mid-crustal shear zone: An integrated EPMA, SIMS, and TIMS study. Chemical Geology, 241, 88–107.

Kabete, J., 2008, A new terrane-based tectonic subdivision of the Archaean Craton and selected belts of Tanzania and its significance to gold metallogeny. PhD thesis, University of Dar es Salaam.

Kabete, J.M., Groves, D.I., McNaughton, N.J., Mruma, A.H., 2012a. A new tectonic and temporal framework for the Tanzanian Shield: Implications for gold metallogeny and undiscovered endowment. Ore Geology Reviews, 48, 88–124.

Kabete, J.M., McNaughton, N.J., Groves, D.I., Mruma, A.H., 2012b, Reconnaissance SHRIMP U-Pb zircon geochronology of the Tanzania Craton: Evidence for Neoarchean granitoid-greenstone belts in the Central Tanzania Region and the Southern East Africa Orogen. Precambrian Research, 216−219, 232−266.

Kazimoto, E., 2008. Study of integrated geochemical techniques in the exploration for gold in North Mara mines, Tanzania. Unpublished MSc. Thesis, University of Dar es Salaam, Dar es Salaam, 208 p.

Kazimoto, E., Schenk, V., 2013. Crustal evolution and hydrothermal gold mineralization in the Paleoproterozoic Katuma Block of the Ubendian Belt, Tanzania. The 24th Colloquium of African Geology, Conference Proceedings, January 8−14, Addis Ababa, Ethiopia.

Kerrich, R., Kyser, T.K., 1994. 100 Ma timing paradox of Archean gold, Abitibi greenstone-belt (Canada) – new evidence from U-Pb and Pb-Pb evaporation ages of hydrothermal zircons. Geology, 22, 1131–1134.

Kerrich, R., Cassidy, K.F., 1994. Temporal relationship of lode gold mineralization to accretion, magmatism, metamorphism and deformation – Archean to present: A review. Ore Geology Reviews, 9, 263–310.

Kerrich, R., Wyman, D., 1990. Geodynamic setting of mesothermal gold deposits: An association with accretionary tectonic regimes. Geology, 18, 882–885.

Kimambo, R.H.N., 1984, Mining and mineral prospects in Tanzania, Eastern Africa Publications Ltd., Arusha, 250 p.

Kreuzer, O.P., 2005, Intrusion-hosted mineralization in the charters towers Goldfield, North Queensland: New isotopic and fluid inclusion constraints on the timing and origin of the auriferous veins. Economic Geology, 100, 1583–1603.

Köner, A., 1984. Late Precambrian plate tectonics and orogeny: A need to redefine the term Pan-African, In: Klerkx, J., Michot, J., (Eds.), African Geology. Tervuren, Musée R. l'Afrique Centrale, 23–28.

Kröner, A., Muhongo, S., Hegner, E., Wingate, M.T.D., 2003. Single-zircon geochronology and Nd isotopic systematics of Proterozoic high-grade rocks from the Mozambique Belt of southern Tanzania (Masasi area): Implications for Gondwana assembly. Journal of the Geological Society, London, 160, 745−757.

Kuehn, S., Ogola, J., Sango, P., 1990. Regional setting and nature of gold mineralization in Tanzania and southwest Kenya. Precambrian Research, 46, 71−82.

Kwelwa, S., Manya, S., Vos, I.M.A., 2013, Geochemistry and petrogenesis of intrusions at the Golden Pride gold deposit in the Nzega greenstone belt, Tanzania. Journal of African Earth Sciences, 86, 53−64

Lang, J.R., Baker, T., 2001. Intrusion-related gold systems: The present level of understanding: Mineralium Deposita, 36, 477 – 489.

Lawley, C.J.M., Selby, D., Imber, J., in press-a, Re-Os molybdenite, pyrite and chalcopyrite geochronology, Lupa Goldfield, SW Tanzania: Tracing metallogenic time scale at mid-crustal shear zones hosting orogenic gold deposits. Economic Geology.

Lawley, C.J.M., Imber, J., Selby, D., in press-b, Structural controls on gold mineralization during transpression: Lupa Goldfield, SW Tanzania. Economic Geology.

Lawley, C.J.M., Selby, D., Condon, D., Morstwood, M., Millar, I., Crowley, Q., Imber, J., 2013, Lithogeochemistry, geochronology and geodynamic setting of the Lupa Terrane, Tanzania:

Implications for the extent of the Archean Tanzanian Craton. Precambrian Research, 231, 174−193.

Lenoir, J.L., Liégeois, J.P., Theunissen, K., Klerkx, J., 1994, The Palaeoproterozoic Ubendian shear Belt in Tanzania: Geochronology and structure. Journal of African Earth Sciences, 19, 169–184.

Li, J.W., Bi, S.J., Selby, D., Chen, L., Vasconcelos, P., Thiede, D., Zhou, M.F., Zhao, X.F., Li, Z.K., Qiu, H.N., 2012. Giant Mesozoic gold provinces related to the destruction of the North China Craton. Earth and Planetary Sciences Letters, 349−250, 26−27.

Lin, S., Corfu, F., 2002. Structural setting and geochronology of auriferous quartz veins at the High Rock Island gold deposit, northwestern Superior Province, Manitoba, Canada. Economic Geology, 97, 43–57.

Ludwig, K.R., 1998. On the treatment of concordant uranium–lead ages: Geochimica et Cosmochimica Acta, 62, 665–676.

Ludwig, K.A. 2008. User's Manual for Isoplot 3.6, A Geochronological Toolkit for Microsoft Excel. Berkeley Geochronology Center Special Publication, No. 4, 77 p.

Manya, S., Kobayashi, K., Maboko, M.A.H., Nakaruma, E., 2006. Ion microprobe zircon U-Pb dating of the late Archaean metavolcanics and associated granites of the Musoma-Mara greenstone belt, Northeast Tanzania: Implications for the geological evolution of the Tanzania Craton. Journal of African Earth Sciences, 45, 355−366.

Manya, S., 2011. Nd-isotopic mapping of the Archaean-Proterozoic boundary in southwestern Tanzania: Implication for the size of the Archaean Tanzania Craton. Gondwana Research, 20, 325−334.

Manya, S., 2012. SHRIMP zircon U-Pb dating of the mafic and felsic intrusive rocks of the Saza area in the Lupa Goldfields, southwestern Tanzania: Implications for gold mineralization. Natural Science, 4, 724–730.

McFarlane, C.R.M., Mavrogenes, J., Lentz, D., King, K., Allibone, A., Holcombe, R., 2011. Geology and intrusion-related affinity of the Morila Gold Mine, southeast Mali. Economic Geology, 106, 727–750.

Möller, A., Mezger, K., Schenk, V., 1998. Crustal age domains and the evolution of the continental crust in the Mozambique Belt of Tanzania: Combined Sm-Nd, Rb-Sr, and Pb-Pb isotopic evidence. Journal of Petrology, 39, 749–783.

Morelli, R., Creaser, R.A., Seltmann, R., Stuart, F.M., Selby, D., Graupner, T., 2007. Age and source constraints for the giant Muruntau gold deposit, Uzbekistan, from coupled Re-Os-He isotopes in arsenopyrite. Geology, 35, 795-798.

Mtoro, M., Maboko, M.A.H., Manya, S., 2009. Geochemistry and geochronology of the bimodal volcanic rocks of the Suguti area in the southern part of the Musoma-Mara Greenstone Belt, Northern Tanzania. Precambrian Research, 174, 241−257.

Oberthur, T., Vetter, U., Davis, D.W., Amanor, J.A., 1998. Age constraints on gold mineralization and Paleoproterozoic crustal evolution in the Ashanti belt of southern Ghana. Precambrian Research, 89, 129–143.

Ootes, L., Lentz, D.R., Creaser, R.A., Ketchum, J.W., Falck, H., 2007. Re-Os molybdenite ages from the Archean Yellowknife greenstone belt comparison to U-Pb ages and evidence for metal introduction at similar to 2675 Ma. Economic Geology, 102, 511–518.

Ootes, L., Morelli, R.M., Creaser, R.A., Lentz, D.R., Falck, H., Davis, W.J., 2011. The timing of Yellowknife gold mineralization a temporal relationship with crustal anatexis. Economic Geology, 106, 713–720.

Parrish, R.R., 2001. The response of mineral chronometers to metamorphism and deformation in orogenic belts. In: Miller, J.A., Holdsworth, R.E., Buck, I.S., & Hand, M. (Eds.), Continental Reactivation and Reworking. Geological Society, London, Special Publications, 184, 289–301.

Pettke, T., Diamond, L.W., Villa, I.M., 1999. Mesothermal gold veins and metamorphic devolatilization in the northwestern Alps: The temporal link. Geology, 27, 641–644.

Phillips, G.N., Powell, R., 2010. Formation of gold deposits; a metamorphic devolatilization model. Journal of Metamorphic Geology, 28, 689–718.

Pinna, P., Muhongo, S., Mcharo, B., Le Goff, E., Deschamps, Y., 2004. Geology and mineral potential of Tanzania : Digital map at 1:2,000,000 scale. Abstract Volume, 20th Colloquium of African Geology, Orleans, France, June 2−7th.

Rasmussen, B., Sheppard, S., Fletcher, I.R., 2006. Testing ore deposit models using in situ U-Pb geochronology of hydrothermal monazite: Paleoproterozoic gold mineralization in northern Australia. Geology, 34, 77–80.

Reddy, S., Collins, A.S., Mruma, A., 2003. Complex high strain deformation in the Usagaran Orogen: Structural setting of Palaeoproterozoic eclogites. Tectonophysics, 375, 101−123.

Ridley, J.R., Diamond, L.W., 2000. Fluid chemistry of orogenic lode gold deposits and implications for genetic models. SEG Reviews, 13, 141–162

Roe, A., Essex, M., 2009. Mining in Tanzania – What future can we expect? The Challenge of mineral wealth: Using resource endowments to foster sustainable development. International Council on Mining and Metals (ICMM) Workshop Paper, Tanzania, 54 p.

Salier, B.P., Groves, D.I., McNaughton, N.J., Fletcher, I.R., 2005. Geochronological and stable isotope evidence for widespread orogenic gold mineralization from a deep-seated fluid source at ca. 2.65 Ga in the Laverton Gold Province, Western Australia. Economic Geology, 100, 1363–1388.

Sarma, S.D., Fletcher, I.R., Rasmussen, B., McNaughton, N.J., Mohan, M.R., Groves, D.I., 2011. Archaean gold mineralization synchronous with late cratonization of the Western Dharwar Craton, India: 2.52 Ga U-Pb ages of hydrothermal monazite and xenotime in gold deposits. Mineralium Deposita, 46, 273–288.

Şener, A.K., Young, C., Groves, D.I., Krapez, B., Fletcher, I.R., 2005. Major orogenic gold episode associated with Cordilleran-style tectonics related to the assembly of Paleoproterozoic Australia? Geology, 33, 225–228.

Schmitz, M.D., Schoene, B., 2007. Derivation of isotope ratios, errors, and error correlations for U-Pb geochronology using ^{205}Pb-^{235}U(^{233}U)-spiked isotope dilution thermal ionization mass spectrometric data. Geochemistry, Geophysics, Geosystems, 8, 20 p.

Scholz, C.H., 1988. The brittle-plastic transition and the depth of seismic faulting. Geologische Rundschau, 77, 319–328.

Sibson, R.H., Robert, F., Poulsen, H., 1988. High-angle reverse faults, fluid-pressure cycling, and mesothermal gold-quartz deposits. Geology, 16, 551–555.

Sillitoe, R.H., Thompson, F.H., 1998. Intrusion-related vein gold deposits: types, tectonomagmatic settings and difficulties of distinction from orogenic gold deposits. Resource Geology, 48, 237–250.

Simpson, R., 2012. NI 43-101 mineral resource estimate update for the Saza-Makongolosi gold project, Tanzania. SRK Consulting, www.helioresource.com, 217 p.

Sommer, H., Kroner, A., Hauzenberger, C., Muhongo, S., 2005a. Reworking of Archean Palaeoproterozoic crust in the Mozambique belt of central Tanzania as documented by SHRIMP zircon geochronology. Journal of African Earth Sciences, 43, 447–463.

Sommer, H., Kröner, A., Muhongo, S., and Hauzenberger, C., 2005b. SHRIMP zircon ages for post-Usagaran granitoid and rhyolitic rocks from the Palaeoproterozoic terrain of southwestern Tanzania. South African Journal of Geology, 108, 247−256.

Stacey, J.S., Kramers, J.D., 1975. Approximation of terrestrial lead isotope evolution by a two-stage model. Earth and Planetary Science Letters, 26, 207–221.

Stein, H.J., Morgan, J.W., Scherstén, 2000. Re-Os dating of low-level highly radiogenic (LLHR) sulfides: The Harnäs gold deposit, southwest Sweden, records continental-scale tectonic events. Economic Geology, 95, 1657–1671.

Stendal, H., Frei, R., Muhongo, S., Ramussen, T.M., Mnali, S., Petro, F., Temu, E.B., 2004. Gold potential of the Mpanda Mineral Field, SW Tanzania: Evaluation based on geological, lead isotopic and aeromagnetic data. Journal of African Earth Sciences, 38, 437–447.

Stern, R.J., 1994. Arc assembly and continental collision in the Neoproterozoic East Africa Orogen: Implications for the consolidation of Gondwanaland. Annual Reviews of Earth and Planetary Sciences, 22, 319–351.

Storey, C.D., Jeffries, T.E., Smith, M., 2006. Common lead-corrected laser ablation ICP-MS U-Pb systematics and geochronology of titanite. Chemical Geology, 227, 37–52.

Tack, L., Wingate, M.T.D., De Waele, B., Meert, J., Belousova, E., Griffin, B., Tahon, A., Fernandez-Alonso, M., 2010. The 1375 Ma "Kibran Event" in central Africa: prominent emplacement of bi-modal volcanism under extensional regime. Precambrian Research, 180, 63–84

Theunissen, K., Klerkx, J., Melnikov, A., Mruma, A., 1996. Mechanisms of inheritance of rift faulting in the western branch of the east African Rift, Tanzania. Tectonics, 15, 776–790.

Thomas, R.J., Roberts, N.M.W., Jacobs, J., Bushi, A.M., Horstwood, M.S.A., Mruma, A., 2013. Structural and geochronological constraints on the evolution of the eastern margin of the Tanzanian Craton in the Mpwapwa area, central Tanzania. Precambrian Research, 224, 671–689

Veilreicher, N.M., Groves, D.I., Snee, L.W., Fletcher, I.R., McNaughton, N.J., 2010. Broad synchroneity of three gold mineralization styles in the Kalgoorlie Gold Field: SHRIMP, U-Pb, and $^{40}Ar/^{39}Ar$ Geochronology Evidence. Economic Geology, 105, 187–227.

Van Straaten,H.P., 1984. Gold mineralization in Tanzania — A review. In: Foster R.P., (Ed.), Gold '82: The Geology, Geochemistry and Genesis of Gold Deposits. Geological Society of Zimbabwe Special Publication no.1, Proceedings of the Symposium Gold ’82, A.A. Balkema/Rotterdam, 673−685.

Von Quadt, A., Erni, M., Martinek, K., Moll, M., Peytcheva, I., Heinrich, C.A., 2011. Zircon crystallization and the lifetimes of ore-forming magmatic-hydrothermal systems. Geology, 39, 731–734.

Vos, I.M.A., Bierlein, F.P., Standing, J.S., and Davidson, G., 2009. The geology and mineralisation at the Golden Pride gold deposit, Nzega Greenstone Belt, Tanzania. Mineralium Deposita, 44, 751−764.

Walraven, F., Pape, J., Borg, G., 1994. Implications of Pb-isotopic compositions at the Geita gold deposit, Sukumaland Greenstone Belt, Tanzania. Journal of African Earth Sciences, 18, 111−121.

Witt, W.K., Vanderhor, F., 1998. Diversity within a unified model for Archaean gold mineralization in the Yilgarn Craton of Western Australia: An overview of the late-orogenic, structurally-controlled gold deposits. Ore Geology Reviews, 13, 29–64.

Yager, T.R., 2010. The Mineral Industry of Tanzania, in 2010 Minerals Yearbook, US Department of the Interior, U.S. Geological Survey, 39.1−39.7.

Figure Captions

Figure 1

Regional geologic map of Tanzania (modified after Pinna et al., 2004; Kabete et al., 2012a). Superterrane abbreviations include (Kabete et al., 2012a, b): East Lake Victoria Superterrane, ELVST; Mwanza-Lake Eyasi Superterrane, MLEST; Lake Nyanza Superterrane, LNST; Moyowosi-Manyoni Superterrane, MMST; Dodoma Basement Superterrane, DBST; Dodoma Schist Superterrane; DSST; Eastern Ubendian-Mtera Superterrane, EUMST; Kalenge-Burigi, KBST, Mbulu-Masai Superterrane, MAST; Kilindi-Handeni Superterrane, KHST; Usagara-Ukaguru Superterrane, UKST; Uluguru-Pare Superterrane; UPST.

Figure 2

Regional geologic map showing the lithotectonic terranes comprising the Palaeoproterozoic Ubendian Belt (modified after Daly, 1988).

Figure 3
Schematic geology map of the Lupa Goldfield (modified after Kimambo, 1984).

Figure 4
Local geology map showing the location of geochronology samples (CL109 and CL0975), mineral systems and artisanal mines. Previously reported U-Pb zircon ages are from Lawley et al. (2013). Eastings and northings are reported as UTM coordinates (WGS84, Zone 36S).

Figure 5
Diagram summarizing previously reported Palaeoproterozoic U-Pb zircon and Re-Os sulphide ages and age ranges, which together with new U-Pb titanite ages, constrain the timing of deformation, magmatism and hydrothermal activity in the Lupa Goldfield. Note the broadly overlapping magmatic and hydrothermal history in the Lupa Goldfield (U-Pb and Re-Os age ranges plotted as horizontal bars; Lawley et al., 2013; Lawley et al., in press-a), whereas individual U-Pb zircon ages (U-Pb zircon ages, without analytical uncertainty, are plotted as vertical bars) show good agreement with three of the temporally distinct hydrothermal events (i.e., ca. 1.95, 1.94, and 1.88 Ga) identified by Re-Os geochronology (weighted average Re-Os ages, without analytical uncertainty, for interpreted hydrothermal events plotted as vertical bars). The ca. 1.88 Ga hydrothermal event is particularly important as it was recorded at all five of the studied gold prospects and also corresponds to the development of D2 auriferous mylonitic shear zones. Note Archaean granites and anomalously younger Mesoproterozoic Re-Os ages are not shown.

Figure 6
(a) Photo of artisanal working along the Kenge shear zone in section view and looking approximately northwest. Fault-fill veins and mylonitic shear zones cut foliated Archaean granite at Kenge; (b) closer photo of fault fill vein and mylonitic shear zone contact at Kenge looking northwest. Note the sharp contact between the mylonite and Archaean granite wall rock (ruler is 15 cm in length); (c) core photo showing complex vein textures that are typical of the fault-fill vein type. Note the laminated vein appearance due to slivers of mylonitized wall rock intercalated

with the fault fill vein; (d–e) core photos of the mineralized zone at Porcupine. Note auriferous quartz veins cutting hydrothermally altered, but non-foliated, Ilunga Syenogranite.

Figure 7

(a) Field photo of foliated Archaean granite sample (CL109); (b) field photo of non-foliated Saza Granodiorite. The Saza Granodiorite is cut by auriferous mylonitic shear zones and quartz veins, but in turns cuts early foliated Archaean granite (not shown). Note overprinting chloritic alteration and en echelon tension gashes; (c) plane polarized light photomicrograph of titanite associated with greenschist facies metamorphic mineral assemblage and tectonic fabric from CL109; (d) plane polarized light photomicrograph of euhedral, and potentially magmatic, titanite crystal from CL0975; (e) stereoscopic photomicrograph showing examples of translucent and fine grained titanite fractions analyzed from CL109; (f) stereoscopic photomicrograph showing examples of fine grained and brown-translucent titanite fractions analyzed from CL0975.

Figure 8

(a–b) Uncorrected (grey ellipses) and corrected [corrected using the Stacey and Kramers (1975) Pb evolution model at 1.9 Ga; S-K; purple ellipses] U-Pb titanite data (purple ellipses) from CL109 and CL0975 on a 2D Terra-Wasserburg plot. Previously reported LA-ICP-MS and ID-TIMS U-Pb zircon ages for CL109 and CL0975, respectively, are also shown for comparison (blue ellipses). The inset figures demonstrate the sensitivity of $^{207}Pb/^{206}Pb$ ages to the assumed isotopic composition of common Pb by varying the Stacey and Kramers (1975) Pb evolution model from 2.5–1.5 Ga. A York Model-1 regression solution of S-K corrected data for CL109 yields an upper intercept U-Pb titanite age of 1921 ± 7 Ma (MSWD = 0.7; n = 7; regression excludes S3 and S4). A York Model-1 regression solution of S-K corrected analyses for CL0975 yields an upper intercept age of 1931 ± 3 Ma (MSWD = 1.1; n =5). The zoomed window in Fig. 6b shows how three of the S-K corrected titanite analyses (purple ellipses) from CL0975 overlap with Concordia and yield a weighted a weighted average $^{207}Pb/^{206}Pb$ age of 1930 ± 3 Ma (MSWD = 0.6; n = 3).

Figure 9

(a–f) Schematic block diagrams showing the geological evolution of the Lupa Goldfield from the Archaean to the Palaeoproterozoic (based on field relationships and U-Pb and Re-Os ages). New U-Pb titanite ages from an Archaean granite suggest that the D1 fabric developed during the Palaeoproterozoic (potentially at ca. 1.92 Ga; Fig. 7e); however the precise timing of D1 remains unclear since Palaeoproterozoic granites (e.g., Ilunga Syenogranite and Saza Granodiorite) are largely non-foliated, which suggests that the D1 fabric locally pre-dated 1.96 Ga (Fig. 7b) and that younger titanite dates may record Pb-loss. Alternatively, D1 may possess a more complex history than previously recognized and may have developed diachronously during the emplacement of Palaeoproterozoic granites (Fig. 7e). Nevertheless, the New U-Pb titanite ages suggest that ductile deformation predated auriferous mylonites by ≥40 Myr. Note Lupa Goldfield's younger geological history is not shown, but anomalous Mesoproterozoic Re-Os ages and lower intercept U-Pb ages provide evidence for a tectono-thermal history spanning multiple orogenic cycles (Lawley et al., 2013; in press-a). Mineralized structures are also locally offset by cataclasites (not shown) and point to a relatively late and dominantly brittle deformation event (D3) of unknown age.

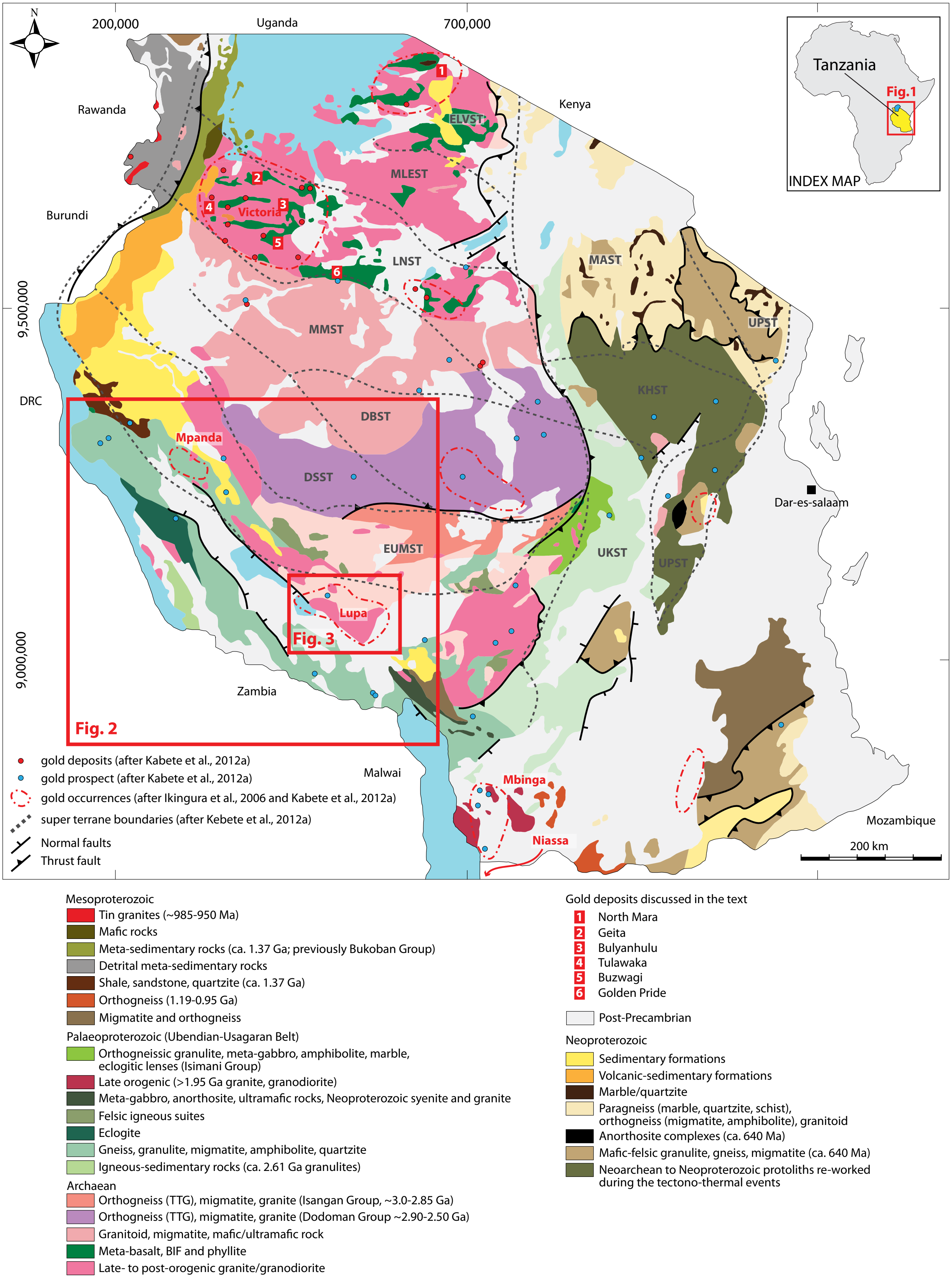
N
200,000
Uganda
700,000
Kenya
Rawanda
Burundi
DRC
Zambia
Malwai
Mozambique
Dar-es-salaam
9,500,000
9,000,000
Tanzania
Fig.1
INDEX MAP
ELVST
MLEST
LNST
MMST
MAST
UPST
KHST
DBST
DSST
EUMST
UKST
Victoria
Mpanda
Lupa
Mbinga
Niassa
Fig. 2
Fig. 3
1
2
3
4
5
6
200 km
gold deposits (after Kabete et al., 2012a)
gold prospect (after Kabete et al., 2012a)
gold occurrences (after Ikingura et al., 2006 and Kabete et al., 2012a)
super terrane boundaries (after Kebete et al., 2012a)
Normal faults
Thrust fault
Mesoproterozoic
Tin granites (~985-950 Ma)
Mafic rocks
Meta-sedimentary rocks (ca. 1.37 Ga; previously Bukoban Group)
Detrital meta-sedimentary rocks
Shale, sandstone, quartzite (ca. 1.37 Ga)
Orthogneiss (1.19-0.95 Ga)
Migmatite and orthogneiss
Palaeoproterozoic (Ubendian-Usagaran Belt)
Orthogneissic granulite, meta-gabbro, amphibolite, marble, eclogitic lenses (Isimani Group)
Late orogenic (>1.95 Ga granite, granodiorite)
Meta-gabbro, anorthosite, ultramafic rocks, Neoproterozoic syenite and granite
Felsic igneous suites
Eclogite
Gneiss, granulite, migmatite, amphibolite, quartzite
Igneous-sedimentary rocks (ca. 2.61 Ga granulites)
Archaean
Orthogneiss (TTG), migmatite, granite (Isangan Group, ~3.0-2.85 Ga)
Orthogneiss (TTG), migmatite, granite (Dodoman Group ~2.90-2.50 Ga)
Granitoid, migmatite, mafic/ultramafic rock
Meta-basalt, BIF and phyllite
Late- to post-orogenic granite/granodiorite
Gold deposits discussed in the text
1 North Mara
2 Geita
3 Bulyanhulu
4 Tulawaka
5 Buzwagi
6 Golden Pride
Post-Precambrian
Neoproterozoic
Sedimentary formations
Volcanic-sedimentary formations
Marble/quartzite
Paragneiss (marble, quartzite, schist), orthogneiss (migmatite, amphibolite), granitoid
Anorthosite complexes (ca. 640 Ma)
Mafic-felsic granulite, gneiss, migmatite (ca. 640 Ma)
Neoarchean to Neoproterozoic protoliths re-worked during the tectono-thermal events

Figure 1

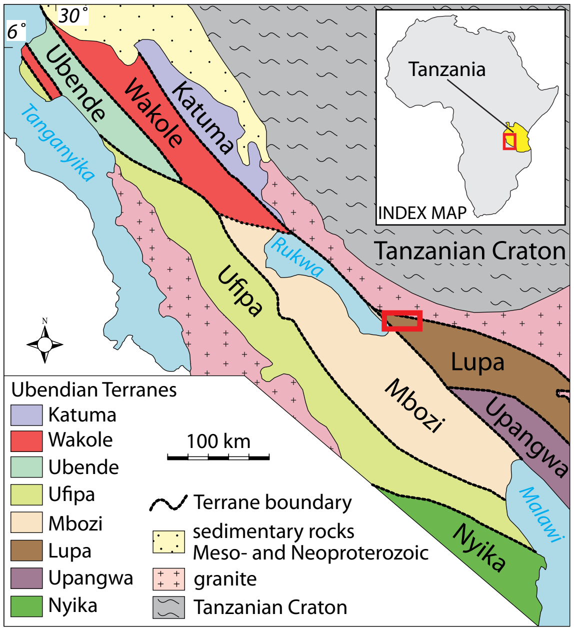

30°
6°
Ubende
Wakole
Katuma
Tanganyika
Tanzania
INDEX MAP
Tanzanian Craton
Rukwa
Ufipa
Lupa
Mbozi
Upangwa
Malawi
Nyika
Ubendian Terranes
Katuma
Wakole
Ubende
Ufipa
Mbozi
Lupa
Upangwa
Nyika
100 km
Terrane boundary
sedimentary rocks
Meso- and Neoproterozoic
granite
Tanzanian Craton

Figure 2

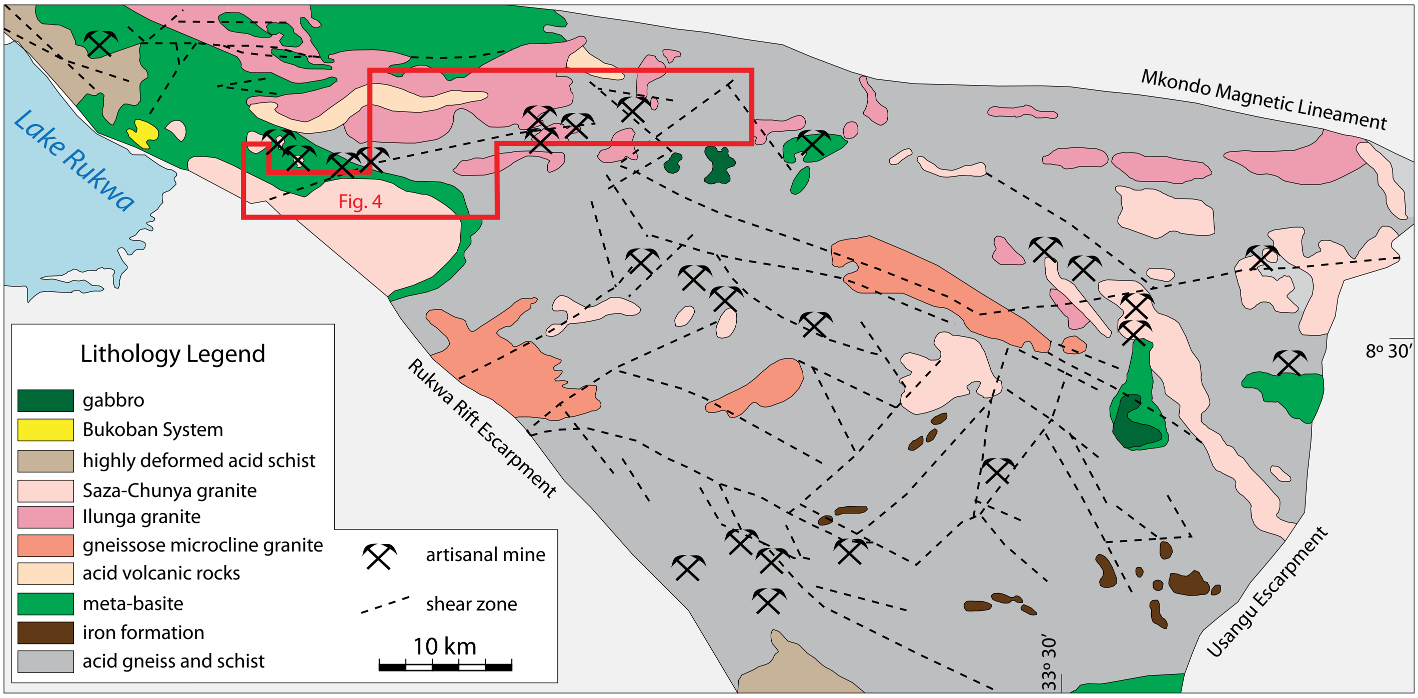

Lake Rukwa
Mkondo Magnetic Lineament
Fig. 4
Rukwa Rift Escarpment
Usangu Escarpment
8º 30′
33º 30′
Lithology Legend
gabbro
Bukoban System
highly deformed acid schist
Saza-Chunya granite
Ilunga granite
gneissose microcline granite
acid volcanic rocks
meta-basite
iron formation
acid gneiss and schist
artisanal mine
shear zone
10 km

Figure 3

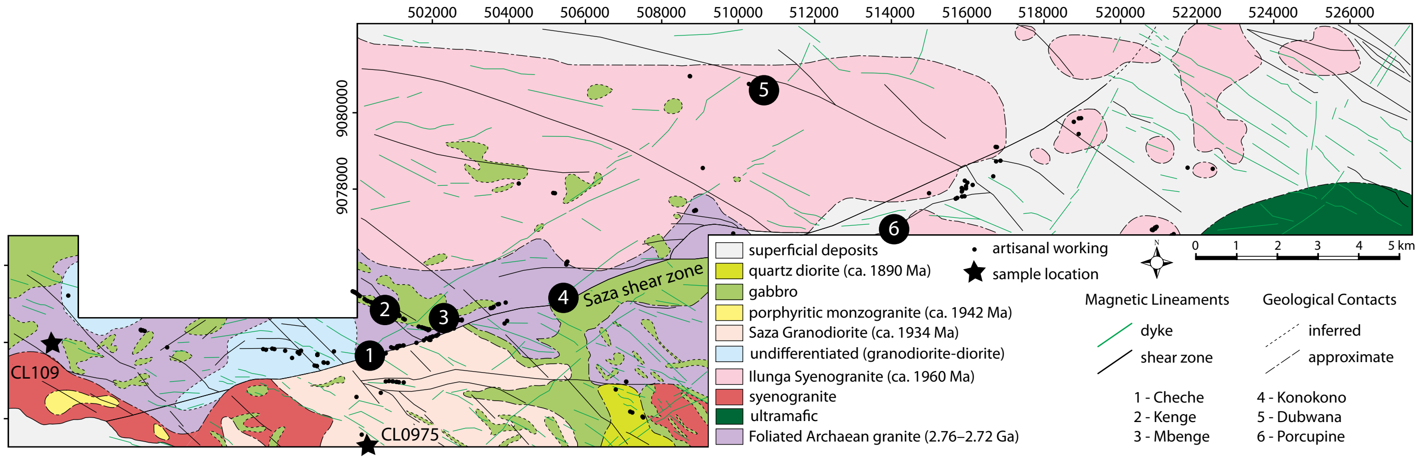
502000
504000
506000
508000
510000
512000
514000
516000
518000
520000
522000
524000
526000
9080000
9078000
9076000
9074000
9072000
Saza shear zone
CL109
CL0975
superficial deposits
quartz diorite (ca. 1890 Ma)
gabbro
porphyritic monzogranite (ca. 1942 Ma)
Saza Granodiorite (ca. 1934 Ma)
undifferentiated (granodiorite-diorite)
Ilunga Syenogranite (ca. 1960 Ma)
syenogranite
ultramafic
Foliated Archaean granite (2.76–2.72 Ga)
artisanal working
sample location
0 1 2 3 4 5 km
Magnetic Lineaments
dyke
shear zone
Geological Contacts
inferred
approximate
1 - Cheche
2 - Kenge
3 - Mbenge
4 - Konokono
5 - Dubwana
6 - Porcupine

Figure 4

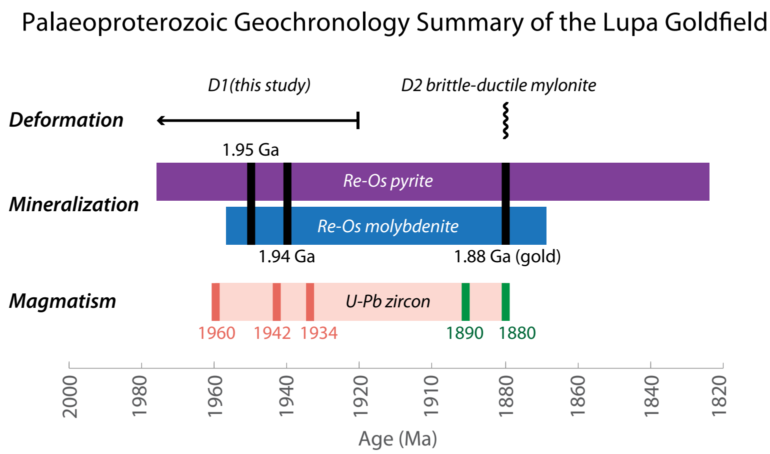
Palaeoproterozoic Geochronology Summary of the Lupa Goldfield
D1 (this study)
D2 brittle-ductile mylonite
Deformation
1.95 Ga
Mineralization
Re-Os pyrite
Re-Os molybdenite
1.94 Ga
1.88 Ga (gold)
Magmatism
U-Pb zircon
1960
1942
1934
1890
1880
2000
1980
1960
1940
1920
1910
1880
1860
1840
1820
Age (Ma)

Figure 5

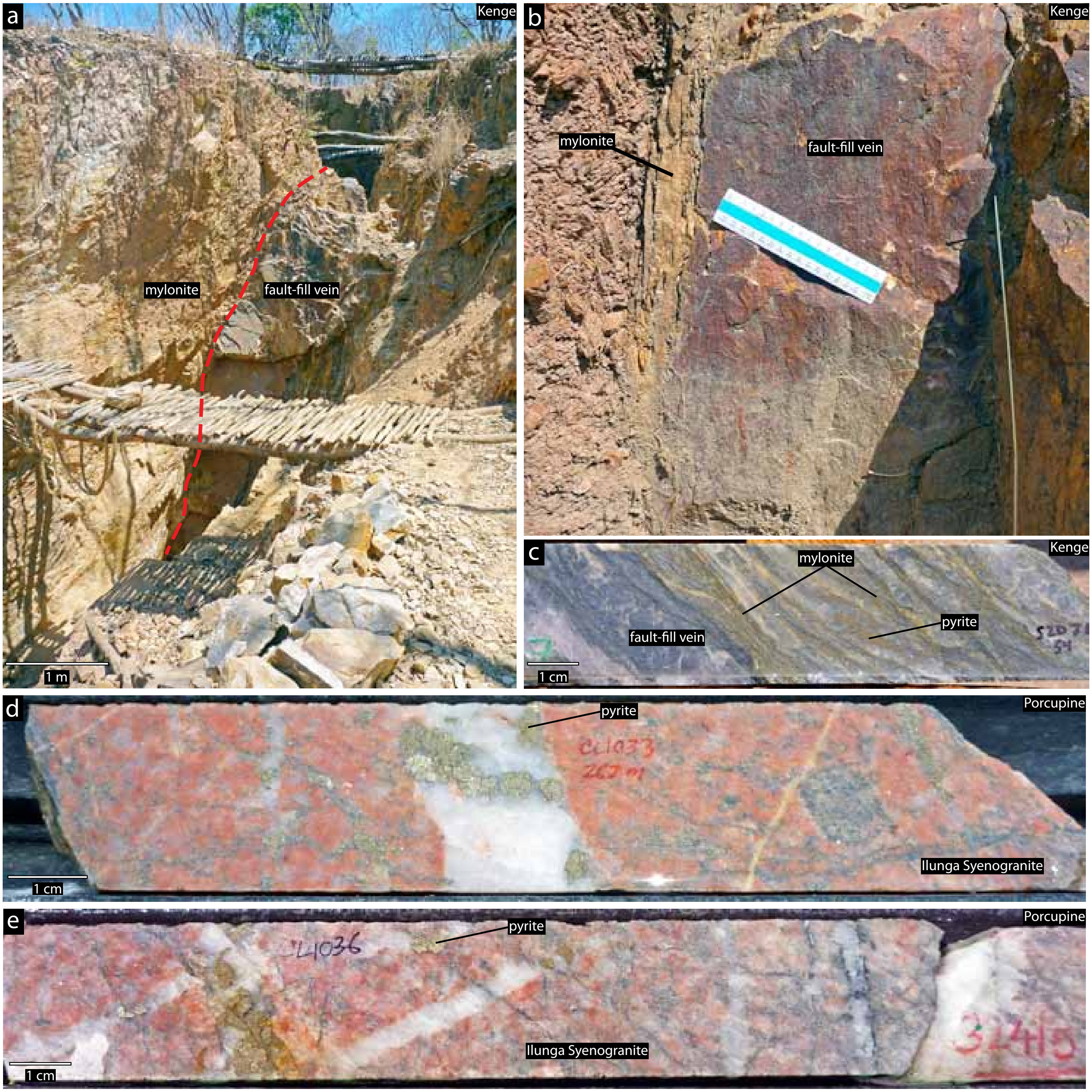
a
Kenge
mylonite
fault-fill vein
1 m
b
Kenge
mylonite
fault-fill vein
c
Kenge
mylonite
pyrite
fault-fill vein
1 cm
d
Porcupine
pyrite
CL1033
1 cm
Ilunga Syenogranite
e
Porcupine
pyrite
CL4036
Ilunga Syenogranite
1 cm

Figure 6

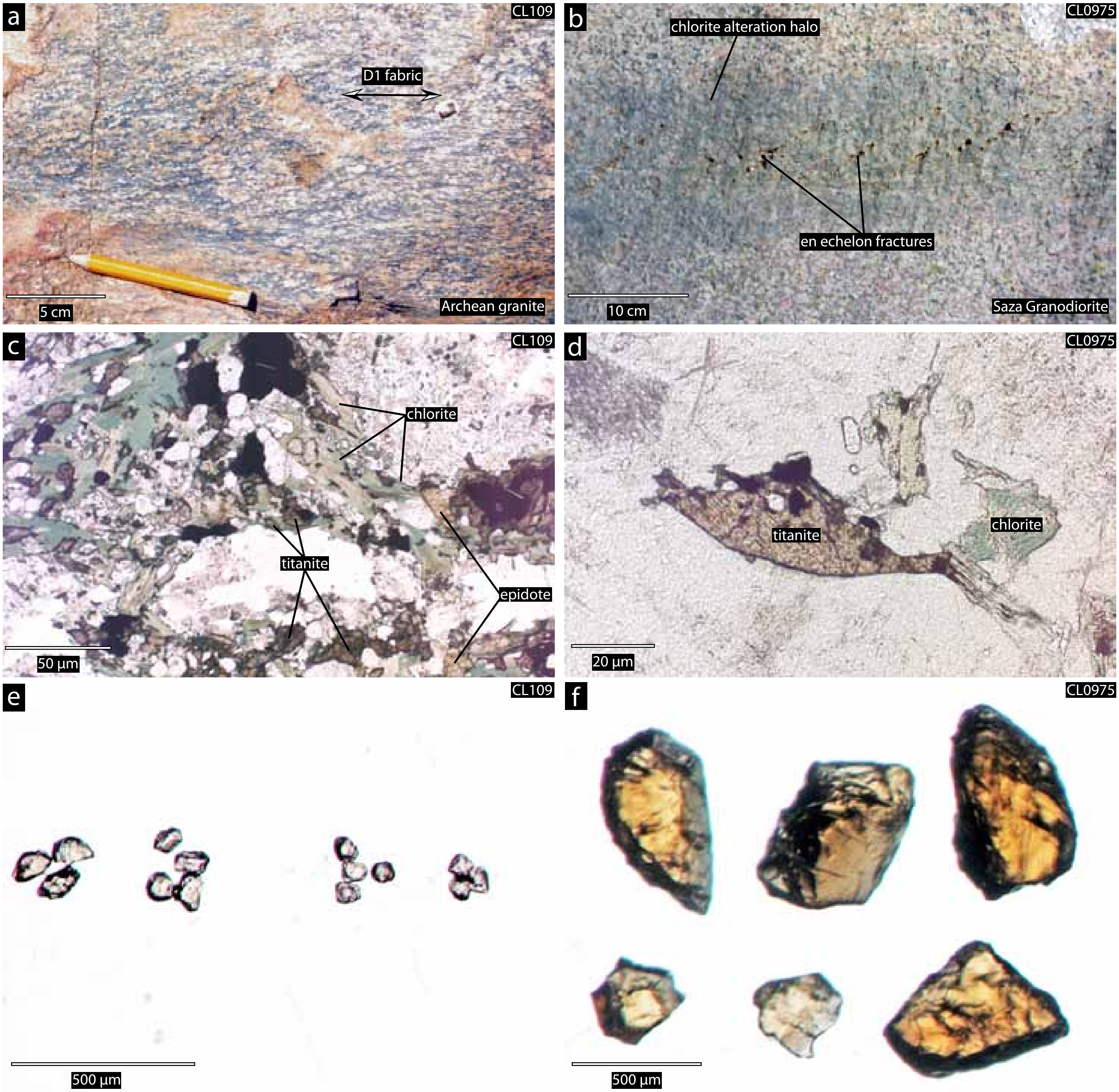
a
CL109
D1 fabric
5 cm
Archean granite
b
CL0975
chlorite alteration halo
en echelon fractures
10 cm
Saza Granodiorite
c
CL109
chlorite
titanite
epidote
50 µm
d
CL0975
titanite
chlorite
20 µm
e
CL109
500 µm
f
CL0975
500 µm

Figure 7

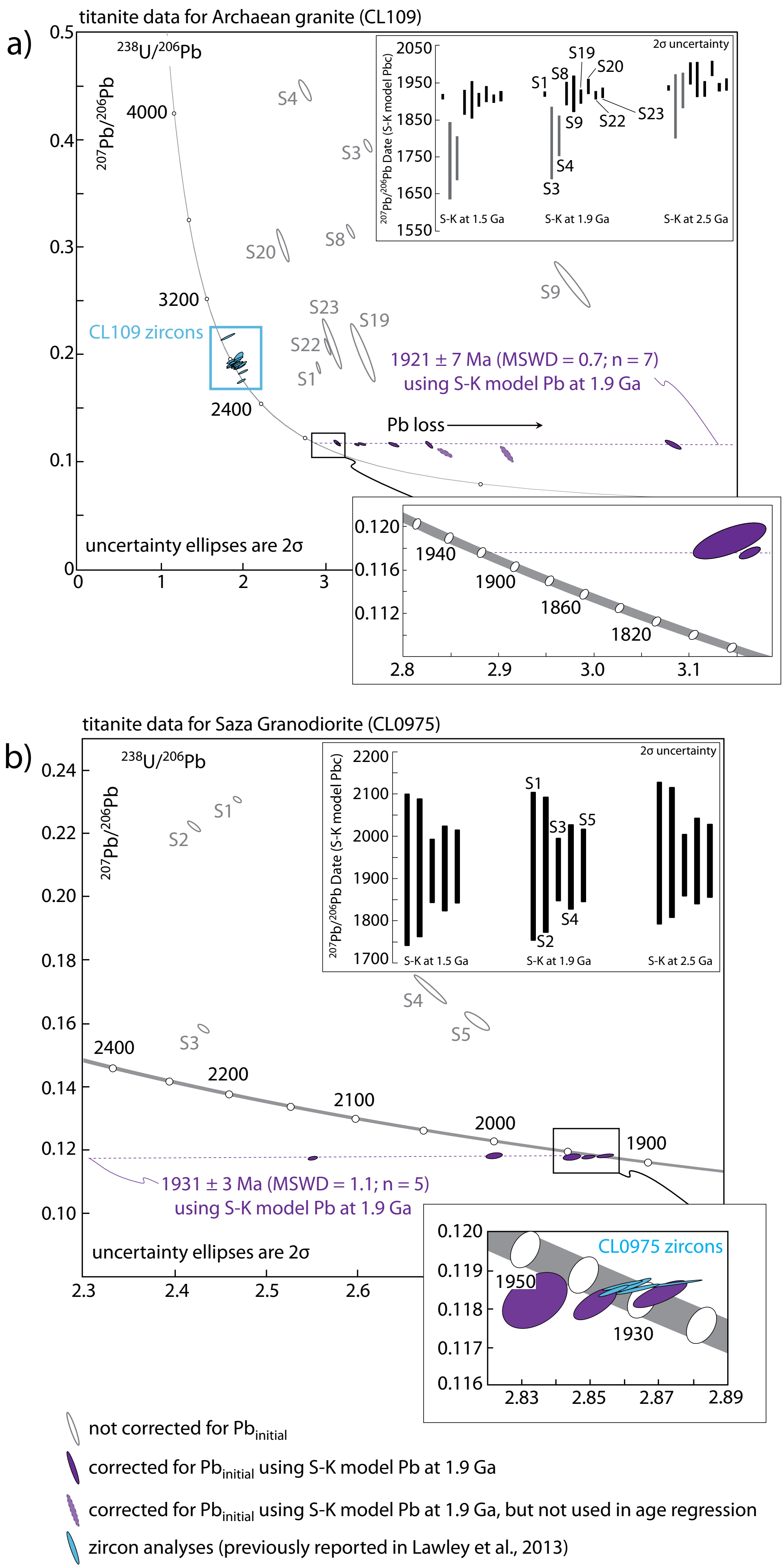
a)
titanite data for Archaean granite (CL109)
$^{238}U/^{206}Pb$
$^{207}Pb/^{206}Pb$
4000
3200
2400
CL109 zircons
S1 S3 S4 S8 S9 S19 S20 S22 S23
1921 ± 7 Ma (MSWD = 0.7; n = 7)
using S-K model Pb at 1.9 Ga
Pb loss
uncertainty ellipses are 2σ
2σ uncertainty
$^{207}Pb/^{206}Pb$ Date (S-K model Pbc)
S-K at 1.5 Ga
S-K at 1.9 Ga
S-K at 2.5 Ga
1940
1900
1860
1820
b)
titanite data for Saza Granodiorite (CL0975)
$^{238}U/^{206}Pb$
$^{207}Pb/^{206}Pb$
2400
2200
2100
2000
1900
S1 S2 S3 S4 S5
1931 ± 3 Ma (MSWD = 1.1; n = 5)
using S-K model Pb at 1.9 Ga
uncertainty ellipses are 2σ
2σ uncertainty
$^{207}Pb/^{206}Pb$ Date (S-K model Pbc)
S-K at 1.5 Ga
S-K at 1.9 Ga
S-K at 2.5 Ga
CL0975 zircons
1950
1930
not corrected for $Pb_{initial}$
corrected for $Pb_{initial}$ using S-K model Pb at 1.9 Ga
corrected for $Pb_{initial}$ using S-K model Pb at 1.9 Ga, but not used in age regression
zircon analyses (previously reported in Lawley et al., 2013)

Figure 8

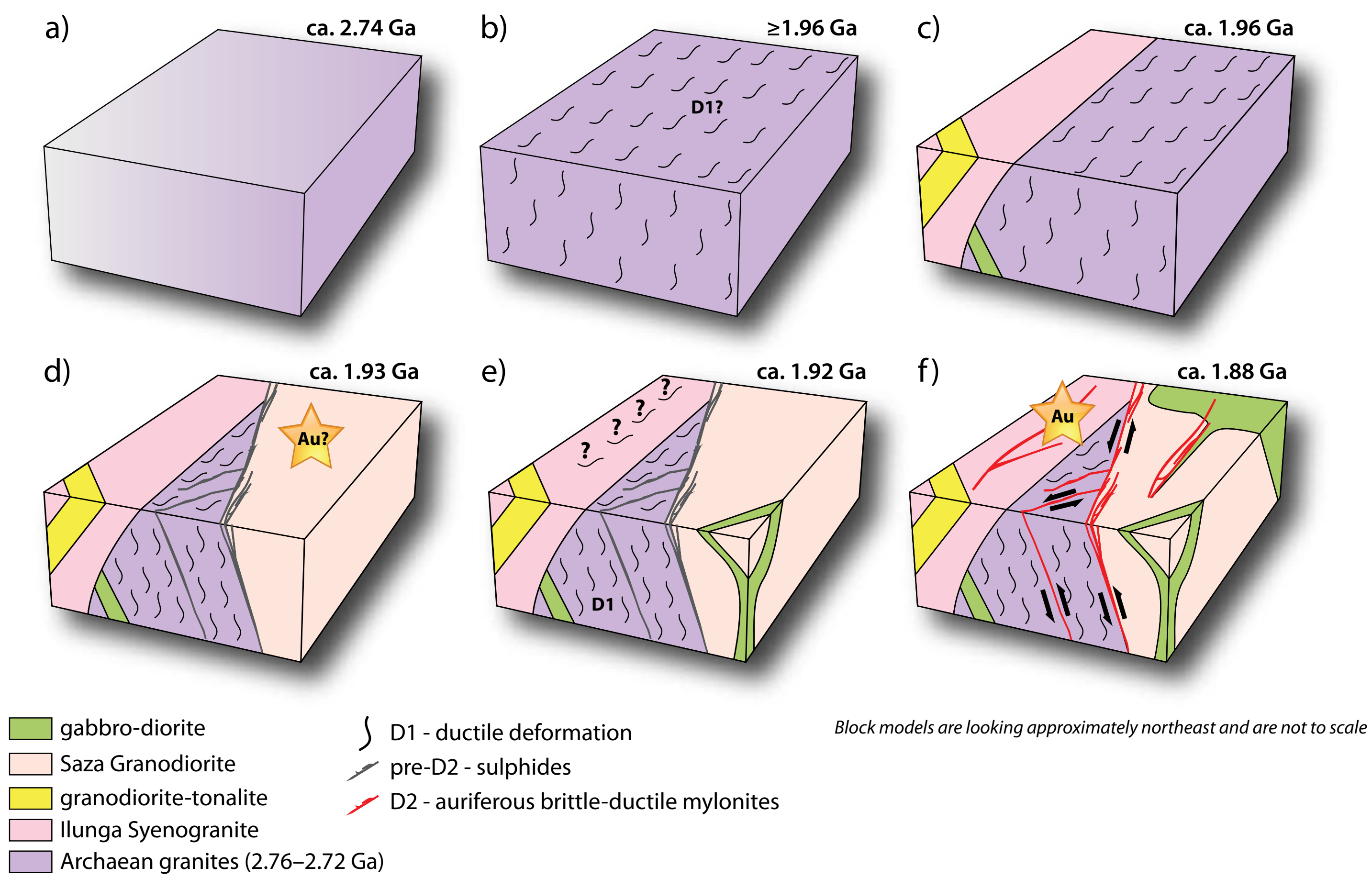
a)
ca. 2.74 Ga
b)
≥1.96 Ga
D1?
c)
ca. 1.96 Ga
d)
ca. 1.93 Ga
Au?
e)
ca. 1.92 Ga
?
D1
f)
ca. 1.88 Ga
Au
gabbro-diorite
Saza Granodiorite
granodiorite-tonalite
Ilunga Syenogranite
Archaean granites (2.76–2.72 Ga)
D1 - ductile deformation
pre-D2 - sulphides
D2 - auriferous brittle-ductile mylonites
Block models are looking approximately northeast and are not to scale

Figure 9

Table 1. U-Th-Pb isotopic data

Sample (a)	Th/U (b)	$^{206}Pb^*$ x10^{-13} mol (c)	mol % $^{206}Pb^*$ (c)	Pb^*/Pbc (c)	Pbc (pg) (c)	$^{206}Pb/^{204}Pb$ (d)	$^{208}Pb/^{206}Pb$ (e)	$^{207}Pb/^{206}Pb$ (e)	% err (f)	$^{207}Pb/^{235}U$ (e)	% err (f)	$^{206}Pb/^{238}U$ (e)	% err (f)	corr. coef.	$^{207}Pb/^{206}Pb$ (g)	± (f)	$^{207}Pb/^{235}U$ (g)	± (f)	$^{206}Pb/^{238}U$ (g)	± (f)
	Compositional Parameters						Radiogenic Isotope Ratios								Isotopic Ages					
CL109																				
s1	8.685	1.8765	91%	9	17	172	2.63713	0.11757	0.37158	5.12124	0.50024	0.31607	0.28828	0.677	1919	7	1840	4	1770	4
s3	5.561	0.9342	66%	1	42	46	2.05308	0.10859	5.43178	2.87496	5.92031	0.19210	1.16198	0.501	1775	99	1375	45	1133	12
s4	8.675	0.4079	60%	1	25	39	3.00279	0.10955	3.04999	3.38886	3.34017	0.22445	1.52124	0.410	1791	56	1502	26	1305	18
s8	10.142	1.0647	76%	3	30	65	3.56932	0.11734	1.77519	3.78833	1.97265	0.23427	0.67383	0.449	1916	32	1590	16	1357	8
s9	6.544	0.3543	78%	3	9	75	2.89817	0.11743	2.74106	2.23765	3.14245	0.13826	1.03516	0.528	1917	49	1193	22	835	8
s19	6.808	0.3295	85%	4	5	107	2.27226	0.11711	1.02463	4.21270	1.77968	0.26101	1.24656	0.827	1912	18	1676	15	1495	17
s20	4.450	0.4556	76%	2	13	65	1.35284	0.11869	1.16054	5.20495	1.56029	0.31821	0.99986	0.669	1936	21	1853	13	1781	16
s22	8.289	1.1981	88%	6	15	131	2.60140	0.11730	0.61527	4.78081	0.77432	0.29572	0.39822	0.616	1915	11	1782	7	1670	6
s23	11.093	0.3767	84%	6	6	105	3.51968	0.11774	0.76732	4.71338	1.43760	0.29046	1.04548	0.855	1922	14	1770	12	1644	15
CL0975																				
s1	7.101	12.6005	87%	5	170	118	2.04070	0.11825	0.50689	5.75101	0.54341	0.35288	0.27228	0.380	1929	9	1939	5	1948	5
s2	7.024	5.5666	88%	5	70	126	1.98811	0.11854	0.46212	5.94430	0.50466	0.36387	0.25145	0.411	1934	8	1968	4	2000	4
s3	6.545	8.6624	95%	13	40	315	1.77382	0.11777	0.21445	6.36479	0.29163	0.39214	0.14130	0.716	1922	4	2027	3	2133	3
s4	7.634	2.3294	93%	10	15	226	2.20028	0.11816	0.28857	5.71131	0.37949	0.35072	0.17821	0.684	1928	5	1933	3	1938	3
s5	6.950	3.5224	94%	13	18	285	2.01251	0.11841	0.24778	5.68564	0.37252	0.34839	0.22256	0.765	1932	4	1929	3	1927	4

Sample (a)	$^{238}U/^{206}Pb$ (h)	% err (f)	$^{207}Pb/^{206}Pb$ (h)	% err (f)	$^{204}Pb/^{206}Pb$ (h)	% err (f)	corr. coef. 8/6-7/6	corr. coef. 8/6-4/6	corr. coef. 7/6-4/6	$^{238}U/^{204}Pb$ (h)	% err (f)	$^{206}Pb/^{204}Pb$ (h)	% err (f)	corr. coef. 8/4-6/4	$^{235}U/^{204}Pb$ (h)	% err (f)	$^{207}Pb/^{204}Pb$ (h)	% err (f)	corr. coef. 5/4-7/4
	Sample (Radiogenic + Initial Pb) Isotope Ratios									Sample (Radiogenic + Initial Pb) Isotope Ratios									
CL109																			
s1	2.90842	0.63551	0.18816	2.11335	0.00525	5.54664	-0.94304	-0.93364	0.99647	553.460993	6.144194	190.296410	5.546638	0.999313	4.015883	6.144194	35.807065	3.445327	0.997181
s3	3.51867	1.01569	0.39489	1.10399	0.02109	1.74569	-0.81246	-0.67796	0.72454	166.806967	2.546213	47.406231	1.745688	0.956041	1.210342	2.546213	18.720344	1.213880	0.628353
s4	2.75546	2.09995	0.44626	1.69109	0.02484	2.19780	-0.87946	-0.86615	0.98221	110.950266	4.151525	40.265570	2.197802	0.967517	0.805049	4.151525	17.968907	0.623712	0.793318
s8	3.30306	0.96507	0.31520	1.52549	0.01472	2.45117	-0.91463	-0.87908	0.95269	224.332673	3.331458	67.916560	2.451167	0.990420	1.627746	3.331458	21.407120	1.100327	0.867201
s9	5.99911	2.93770	0.26660	6.28610	0.01110	11.09868	-0.97046	-0.96419	0.99294	540.393150	13.952954	90.078859	11.098684	0.998440	3.921064	13.952954	24.014967	4.913830	0.983361
s19	3.45787	3.49886	0.20239	10.74043	0.00634	25.09789	-0.95339	-0.95246	0.99918	545.070753	28.450395	157.631917	25.097887	0.999298	3.955004	28.450395	31.902666	14.372904	0.998682
s20	2.48128	2.24673	0.30248	3.84972	0.01370	6.22461	-0.93974	-0.93702	0.99762	181.144783	8.366722	73.004701	6.224608	0.995592	1.314377	8.366722	22.082102	2.398797	0.987342
s22	3.02946	0.95581	0.20839	2.82371	0.00678	6.36678	-0.95466	-0.94810	0.99587	446.960561	7.279330	147.537871	6.366777	0.999128	3.243122	7.279330	30.745556	3.563952	0.995452
s23	3.07716	3.01549	0.21060	8.82788	0.00691	19.70896	-0.95833	-0.95740	0.99936	445.127104	22.612749	144.655189	19.708961	0.999258	3.229818	22.612749	30.464599	10.891381	0.998668
CL0975																			
s1	2.46803	0.14137	0.23103	0.24519	0.00840	0.49173	-0.73746	-0.36875	0.75343	293.758217	0.559511	119.025226	0.491732	0.972030	2.131494	0.559511	27.498842	0.346756	0.778471
s2	2.42092	0.21977	0.22257	0.55365	0.00775	1.16458	-0.91991	-0.81574	0.95534	312.275906	1.349856	128.990334	1.164580	0.995556	2.265857	1.349856	28.709537	0.656374	0.944823
s3	2.43100	0.17231	0.15861	0.59326	0.00304	2.25488	-0.83437	-0.74161	0.97755	799.518730	2.385468	328.884369	2.254876	0.998825	5.801265	2.385468	52.164448	1.679597	0.993264
s4	2.67886	0.50225	0.17101	1.96415	0.00394	6.25903	-0.98383	-0.97258	0.99661	680.509624	6.748516	254.029522	6.259025	0.999850	4.937741	6.748516	43.441625	4.304555	0.998652
s5	2.73024	0.38223	0.16105	1.41795	0.00318	5.28003	-0.87134	-0.85159	0.99345	859.439228	5.609118	314.785585	5.280033	0.999362	6.236045	5.609118	50.696522	3.874763	0.997856

(a) z1, z2 etc. are labels for fractions composed of single zircon grains or fragments; all fractions annealed and chemically abraded after Mattinson (2005).

(b) Model Th/U ratio calculated from radiogenic $^{208}Pb/^{206}Pb$ ratio and $^{207}Pb/^{235}U$ age.

(c) Pb* and Pbc represent radiogenic and common Pb, respectively; mol % $^{206}Pb^*$ with respect to radiogenic, blank and initial common Pb.

(d) Measured ratio corrected for spike and fractionation only.
Daly analyses, based on analysis of NBS-981 and NBS-982.

(e) Corrected for fractionation, spike, and common Pb; up to 1 pg of common Pb was assumed to be procedural blank: $^{206}Pb/^{204}Pb = 18.60 \pm 0.80\%$; $^{207}Pb/^{204}Pb = 15.69 \pm 0.32\%$;
$^{208}Pb/^{204}Pb = 38.51 \pm 0.74\%$ (all uncertainties 1-sigma). Excess over blank was assigned to initial common Pb.

(f) Errors are 2-sigma, propagated using the algorithms of Schmitz and Schoene (2007) and Crowley et al. (2007).

(g) Calculations are based on the decay constants of Jaffey et al. (1971). $^{206}Pb/^{238}U$ and $^{207}Pb/^{206}Pb$ ages corrected for initial disequilibrium in $^{230}Th/^{238}U$ using Th/U [magma] = 3.

(h) Corrected for fractionation, spike, and blank Pb only.

Table 3. Summary of geologic characteristics at Tanzanian gold deposits and goldfields

Goldfield/Region	Significant Deposits	Host Rock	Host Rock Age (Ga)	Ore Controls	Hydrothermal Alteration Mineral Assemblage	Metamorphic facies	Metals	Sulphide Assemblage	Gold (Ga)	Method	Source
Goldfields within the Tanzanian Craton											
Lake Victoria	North Mara	sedimentary and volcanic rocks, granodiorite, tonalite, porphyritic andesite/dacite, gabbro	2.76−2.65	shear and quartz vein hosted; lithologic contact control	Ser ± Chl ± Carb ± Sil ± Pot ± Sod	greenschist	Au ± Cu	Py ± Cpy ± Po	2.69−2.64	constrained by U-Pb zircon dating of magmatism and/or deformation	Manya et al., 2006; Kabete, 2008; Kazimoto, 2008; Mtoro et al., 2009; Ikingura et al., 2009
Lake Victoria	Geita	BIF, felsic-mafic volcanic and sedimentary rocks	2.84−2.64	BIF, fault and quartz vein control	Carb ± Sil ± ?	amphibolite to greenschist	Au	Py ± Po ± Cpy ± Asp	≤2.644	U-Pb zircon dating of pre-gold lamprophyre dike	Walraven and Borg, 1994; Borg and Krough, 1999; Kabete et al., 2012a
Lake Victoria	Bulyanhulu	sedimentary (including graphitic argillite), and felsic-mafic volcanic rocks	2.84−2.64	shear (breccia) and quartz vein hosted; lithologic contact control	Ser ± Chl ± Carb ± Sil	greenschist	Au ± Cu ± Pb	Py ± Po ± Asp ± Cpy ± Gal	2.69−2.63	constrained by U-Pb zircon dating of magmatism and/or deformation	Chamberlain, 2003; Kabete et al., 2012a
Lake Victoria	Tulawaka	mafic-felsic volcanic and sedimentary rocks, granite, aplite dikes	2.84−2.64	shear and quartz vein hosted; lithologic contact control	?	amphibolite to greenschist	Au	?	2.69−2.63	constrained by U-Pb zircon dating of magmatism and/or deformation	Cloutier et al., 2005; Kabete et al., 2012a
Lake Victoria	Buzwagi	granite and lesser mafic volcanic rocks	2.84−2.64	shear and quartz vein hosted	Ser ± Sil ± ?	greenschist	Au ± Cu	Py ± Cpy	2.69−2.63	constrained by U-Pb zircon dating of magmatism and/or deformation	Ikingura et al., 2009
Lake Victoria	Golden Pride	sedimentary (predominately sandstone/siltstone) rocks, BIF, dacitic intrusions	2.7 to <2.65	shear and quartz vein hosted; lithologic control	Ser ± Chl ± Carb ± Biot ± Cltd	greenschist	Au	Po + Asp + Py + Cpy ± Gal ± Sph ± Stb ± Tel ± Co-Ni-Bi sulphides	ca. 2.68	U-Pb dating of co-genetic magmatic phases	Vos et al., 2009; Kwelwa et al., 2012a
Central Tanzania	mainly artisanal workings	amphibolite, granitic gneisses; mafic volcanic and sedimentary rocks (including BIF)	2.82−2.66	shear and quartz vein hosted	Sil ± Pot ± Chl	amphibolite to greenschist	Au	Py ± ?	2.70−2.66	constrained by U-Pb zircon dating of magmatism and/or deformation	Kabete et al., 2012a
Goldfields at cratonic margins											
Lupa	Kenge Mbenge Porcupine	granite, granodiorite, gabbro	2.76−1.88	shear and quartz vein hosted; lithologic contact control	Ser ± Chl ± Carb ± Sil	greenschist	Au	Py ± Cpy ± Gal ± Mo ± Sph	ca. 1.88	Re-Os pyrite	Lawley et al., in press
Mpanda	mainly artisanal workings	orthogneisses, metapelites, metabasites, gabbro	2.65−1.93	shear and quartz vein hosted	Ser ± Chl ± Carb	granulite to greenschist	Pb ± Cu ± Au ± Ag	Gal + Cpy + Py	ca. 1.2? ca. 0.72?	U-Pb monazite Pb-Pb galena	Kuehn et al., 1990; Stendal et al., 2004; Kazimoto and Schenk, 2013
Niassa	mainly artisanal workings	sedimentary rocks, gabbro	ca. 0.714	shear and quartz vein hosted	Chl ± Carb ± Grun ± Ser	greenschist	Au	Py ± Cpy ± Mar ± Po ± Sph	ca. 0.483	Re-Os pyrite	Bjerkgard et al., 2009
Burundi	mainly artisanal workings	volcanic and sedimentary rocks, granite	1.78−1.37	shear, quartz vein, and breccia hosted	Ser ± Tour ± Oxides	greenschist	Au ± Sn ± W ± Bi	Py ± Asp ± Cpy ± Bi-sulphides ± oxides (cassiterite ± hematite)	ca. 1.0−0.9 ca. 0.64	Rb-Sr whole rock, muscovite, and tourmaline	Brinckmann et al., 1994; Fernandez-Alonso et al., 2012

List of abbreviations used. Hydrothermal alteration mineral assemblage: Ser = sercitie, Chl = chlorite, Carb = carbonate mienrals, Sil = silica flooding, Grun = grunerite, Pot = potassic, Sod = sodic, Cltd = chloritoid, Tour = tourmaline, Oxides = oxide minerals. Sulphide Assemblage: Py = pyrite, Cpy = chalcopyrite, Po = pyrrhotite, Asp = arsenopyrite, Gal = galena, Sph = sphalerite, Stb = stibnite, Tel = telurides, Mo = molybdenite, Mar = marcasite.

Table. 1 - Geochronology Summary

Sample ID	Sample type	Analysis method		Interpreted age (Ma)	Analytical Uncertainty at 2σ (Ma)	Age determination method
CL0975	Saza Granodiorite	U-Pb zircon[1]	ID-TIMS	1934.5	1.0	weighted average $^{207}Pb/^{206}Pb$ concordant zircon age
CL0972	Ilunga Syenogranite	U-Pb zircon[1]	ID-TIMS	1959.6	1.1	weighted average $^{207}Pb/^{206}Pb$ concordant zircon age
CL0911	granodiorite dike cutting foliated granite (CL098)	U-Pb zircon[1]	ID-TIMS	1958.5	1.3	weighted average $^{207}Pb/^{206}Pb$ concordant zircon age
CL098	foliated granite	U-Pb zircon[1]	LA-MC-ICP-MS	2723	10	weighted average $^{207}Pb/^{206}Pb$ concordant zircon age
CL1020	foliated granite	U-Pb zircon[1]	LA-MC-ICP-MS	2739	10	weighted average $^{207}Pb/^{206}Pb$ concordant zircon age
CL109	foliated granite	U-Pb zircon[1]	LA-MC-ICP-MS	2758	9	weighted average $^{207}Pb/^{206}Pb$ concordant zircon age
CL1019	porphyritic monzogranite	U-Pb zircon[1]	LA-MC-ICP-MS	1942	14	weighted average $^{207}Pb/^{206}Pb$ concordant zircon age
CL1021	quartz diorite	U-Pb zircon[1]	LA-MC-ICP-MS	1891	17	upper intercept Concordia age
CL1022	gabbroic dike cutting foliated granite (CL109)	U-Pb zircon[1]	LA-MC-ICP-MS	1880	17	upper intercept Concordia age
multiple samples	ultrafine molybdenite from Kenge	Re-Os molybdenite[2]	N-TIMS	1953	6	weighted average Re-Os model age
multiple samples	molybdenite from Kenge	Re-Os molybdenite[2]	N-TIMS	1937	4	weighted average Re-Os model age
multiple samples	pyrite from mylonitic shear zone at Kenge and Mbenge	Re-Os pyrite[2]	N-TIMS	1876	10	weighted average Re-Os model age
multiple samples	pyrite and chalopyrite from quartz veins at Kenge	Re-Os pyrite chalcopyrite[2]	N-TIMS	1953	37	weighted average Re-Os model age
multiple samples				1871	12	
multiple samples				1885	9	
multiple samples	pyrite and chalcopyrite from quartz veins at Konokono	Re-Os pyrite chalcopyrite[2]	N-TIMS	1371	160	weighted average Re-Os model age
multiple samples				975	6	
multiple samples	ultrafine molybdenite from Porcupine	Re-Os molybdenite[2]	N-TIMS	1886	6	weighted average Re-Os model age
multiple samples	molybdenite from Porcupine	Re-Os molybdenite[2]	N-TIMS	1873	5	weighted average Re-Os model age
multiple samples				1894	45	
multiple samples	pyrite from Porcupine	Re-Os pyrite[2]	N-TIMS	1057	56	weighted average Re-Os model age
multiple samples				922	190	
multiple samples	pyrite from Dubwana	Re-Os pyrite[2]	N-TIMS	1910	38	individual Re-Os model ages
multiple samples				1900	38	
CL109	foliated granite	U-Pb titanite[3]	ID-TIMS	1921	7	upper intercept Concordia age
CL0975	Saza Granodiorite	U-Pb titanite[3]	ID-TIMS	1930	3	weighted average $^{207}Pb/^{206}Pb$ concordant titanite age

[1]Data takern from Lawley et al., 2013
[2]Data taken from Lawley et al., in press-a
[3]Data from this study